The Astrophysical Journal, 968:69 (23pp), 2024 June 20 https://doi.org/10.3847/1538-4357/ad3961

Atmospheric Limitations for High-frequency Ground-based Very Long Baseline Interferometry

Dominic W. Pesce[1,2], Lindy Blackburn[1,2], Ryan Chaves[1], Sheperd S. Doeleman[1,2], Mark Freeman[1], Sara Issaoun[1,2], Michael D. Johnson[1,2], Greg Lindahl[1,3], Iniyan Natarajan[1,2], Scott N. Paine[1], Daniel C. M. Palumbo[1,2], Freek Roelofs[1,2], and Paul Tiede[1,2]
[1] Center for Astrophysics | Harvard & Smithsonian, 60 Garden Street, Cambridge, MA 02138, USA; dpesce@cfa.harvard.edu
[2] Black Hole Initiative at Harvard University, 20 Garden Street, Cambridge, MA 02138, USA
[3] Common Crawl Foundation, 9663 Santa Monica Boulevard #425, Beverly Hills, CA 90210, USA
Received 2024 January 24; revised 2024 March 6; accepted 2024 March 31; published 2024 June 11

Abstract

Very long baseline interferometry (VLBI) provides the highest-resolution images in astronomy. The sharpest resolution is nominally achieved at the highest frequencies, but as the observing frequency increases, so too does the atmospheric contribution to the system noise, degrading the sensitivity of the array and hampering detection. In this paper, we explore the limits of high-frequency VLBI observations using `ngehtsim`, a new tool for generating realistic synthetic data. `ngehtsim` uses detailed historical atmospheric models to simulate observing conditions, and it employs heuristic visibility detection criteria that emulate single- and multifrequency VLBI calibration strategies. We demonstrate the fidelity of `ngehtsim's` predictions using a comparison with existing 230 GHz data taken by the Event Horizon Telescope (EHT), and we simulate the expected performance of EHT observations at 345 GHz. Though the EHT achieves a nearly 100% detection rate at 230 GHz, our simulations indicate that it should expect substantially poorer performance at 345 GHz; in particular, observations of M87* at 345 GHz are predicted to achieve detection rates of $\lesssim$20% that may preclude imaging. Increasing the array sensitivity through wider bandwidths and/or longer integration times—as enabled through, e.g., the simultaneous multifrequency upgrades envisioned for the next-generation EHT—can improve the 345 GHz prospects and yield detection levels that are comparable to those at 230 GHz. M87* and Sgr A* observations carried out in the atmospheric window around 460 GHz could expect to regularly achieve multiple detections on long baselines, but analogous observations at 690 and 875 GHz consistently obtain almost no detections at all.

Unified Astronomy Thesaurus concepts: Long baseline interferometry (932); Very long baseline interferometry (1769); Radio interferometry (1346); Submillimeter astronomy (1647); Astronomy data modeling (1859)

1. Introduction

The history of very long baseline interferometry (VLBI) has seen a progression toward observations at ever-higher frequencies. Beginning with a series of early results spanning frequencies lower than 1 GHz up to 22 GHz (Bare et al. 1967; Broten et al. 1967; Moran et al. 1967; Burke et al. 1970), important milestones have included the first VLBI detections at frequencies of 43 GHz (Moran et al. 1979), 89 GHz (Readhead et al. 1983), and 223 GHz (Padin et al. 1990). The Event Horizon Telescope (EHT) currently executes the highest-frequency VLBI observations of any existing array, and EHT observations at a frequency of ∼230 GHz have demonstrated the unique science opportunities accessible to an instrument capable of imaging with an angular resolution of ∼20 μas. EHT images of M87* (Event Horizon Telescope Collaboration et al. 2019a, 2019b, 2019c, 2019d, 2019e, 2019f, 2021a, 2021b, 2023) and Sgr A* (Event Horizon Telescope Collaboration et al. 2022a, 2022b, 2022c, 2022d, 2022e, 2022f) currently provide our only event-horizon-scale views of the emission region in the immediate vicinity of a black hole.

It is notable that the amount of time separating the first successful VLBI observations at any wavelength (conducted in 1967) and the first VLBI detections at a wavelength of ∼1.3 mm (for which the observations were conducted in 1989) was shorter than the amount of time separating the first 1.3 mm detections and the first 1.3 mm images (for which the observations were conducted in 2017). This seeming discrepancy provides some indirect evidence for the many practical difficulties facing high-frequency VLBI observations, which must contend with smaller typical aperture sizes, higher characteristic system noise temperatures, increased atmospheric attenuation, and shorter atmospheric coherence times than analogous observations conducted at lower frequencies. The decades preceding the first EHT results saw substantial developments in broadband instrumentation, with the explicit aim of overcoming these difficulties through improvements to the instantaneous sensitivity of the array (Doeleman et al. 2008; Whitney et al. 2013; Vertatschitsch et al. 2015; Matthews et al. 2018; Event Horizon Telescope Collaboration et al. 2019b).

Difficulties notwithstanding, the allure of high-frequency VLBI observations continues to motivate developments that push the frontier. The EHT has already carried out VLBI observations at 345 GHz (Crew et al. 2023; A. W. Raymond et al. 2024, in preparation), and the next-generation EHT project seeks to substantially build out the array (Doeleman et al. 2019, 2023): increasing the bandwidth, placing multiple new dishes at locations that fill gaps in the existing coverage, and adopting simultaneous multifrequency observing capabilities that aim to make 345 GHz observations more commonplace. Furthermore, there are aspirations for at least a subset of

the stations to carry out VLBI at frequencies as high as 690 GHz (e.g., Inoue et al. 2014). Maximizing the potential success of such endeavors, as well as making decisions about the optimal locations of new dishes and which technological developments to prioritize, requires an informed understanding of how array upgrades and operational choices will manifest in the collected data.

A number of synthetic data generation tools have been developed and used within the high-frequency VLBI community to address such considerations. In addition to predicting future capabilities, synthetic data are important for developing imaging and calibration algorithms (e.g., Roelofs et al. 2023) and even for analyzing existing data (e.g., Event Horizon Telescope Collaboration et al. 2019d, 2022c). Two synthetic data tools that have seen substantial use within the EHT collaboration are `ehtim` (Chael et al. 2016, 2018, 2023) and `SYMBA` (Roelofs et al. 2020). `ehtim` is foremost an image reconstruction software, but it also includes a suite of easy-to-use synthetic observation and data handling abilities. `ehtim` provides rapid (typically ∼seconds) data generation with a simple user interface. However, it does not directly simulate many effects (particularly those associated with the atmosphere) that are relevant for determining array sensitivity. In contrast, `SYMBA` was developed for end-to-end synthetic data generation from the start; it leverages `MeqSilhouette` (Blecher et al. 2017; Natarajan et al. 2022) to simulate physically realistic atmospheric and instrumental effects, and it passes all data through the `rPICARD` VLBI calibration pipeline (Janssen et al. 2019). By mirroring the same processes that are applied to real VLBI data, `SYMBA` aims to maximize realism at the cost of increased runtime (typically tens of minutes to hours, depending on the generated data volume) and requisite user sophistication relative to `ehtim`.

In this paper, we introduce `ngehtsim`,[4] a Python-based tool for simulating radio interferometric data that builds on the work of Raymond et al. (2021) to incorporate realistic atmospheric conditions and visibility detection criteria. `ngehtsim` aims to retain the speed and user-friendliness of synthetic data generation tools like `ehtim` while striving for the physical realism of tools like `SYMBA`. Relevant atmospheric properties are pretabulated and stored within the `ngehtsim` codebase, which both serves as a centralized repository of weather information and reduces computational overhead during synthetic data generation. `ngehtsim` also employs heuristic visibility detection schemes that emulate VLBI calibration strategies relevant for high-frequency and multi-frequency observations without requiring the running of a full calibration pipeline.

This paper is organized as follows. In Section 2, we describe our procedure for generating atmospheric spectra, and in Section 3, we describe how the synthetic interferometric data are generated. In Section 4, we provide several examples of `ngehtsim` synthetic data generation, focusing primarily on EHT observations at frequencies of 230 GHz and above. We summarize and conclude in Section 5.

2. Simulating Atmospheric Conditions

The primary atmospheric quantities that determine the sensitivity of radio astronomical observations are the optical depth (τ) and the brightness temperature (T_b). From the optical depth, the atmospheric transmittance is given by $e^{-\tau}$ and quantifies the amount of incident radiation that gets absorbed or scattered by the atmosphere. We use version 12.2 of the *am* radiative transfer software (Paine 2022) to compute atmospheric optical depth and brightness temperature as a function of frequency (ν).

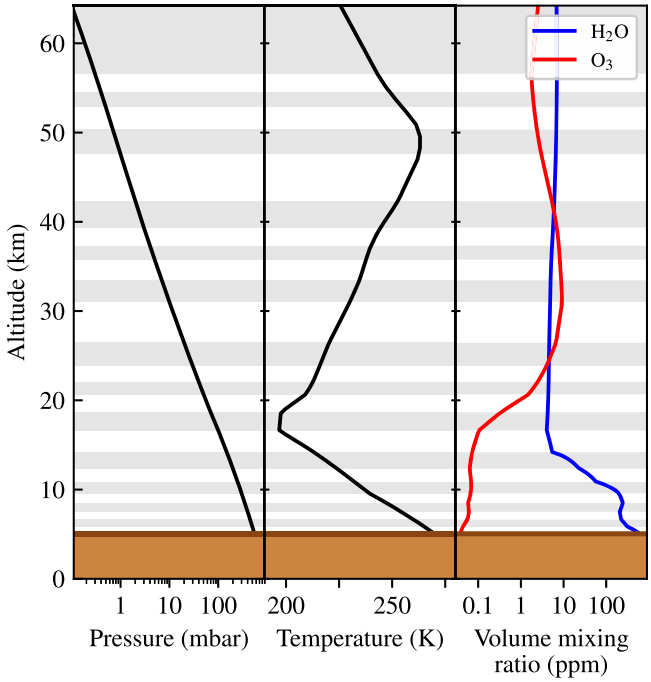

Figure 1. Atmospheric state above the ALMA site at (latitude, longitude) = (−23.°032, −67.°755) and elevation of 5040 m, taken from the 2022 April 15 MERRA-2 reanalysis at 0 UTC. From left to right, the quantities plotted are the pressure in millibar (mbar), the temperature in K, and the volume mixing ratio of H_2O (in blue) and O_3 (in red) in parts per million (ppm); all quantities are plotted as a function of altitude. The alternating white and gray shading indicates the locations of the individual atmospheric layers, and the brown shaded region on the bottom indicates the ground level.

2.1. Weather Data and Atmospheric Spectra

The *am* software takes as its primary inputs the pressure, temperature, and composition at each of a user-defined number of layers in the atmosphere. We set the temperature of the radiation that is incident onto the upper atmospheric layer equal to the cosmic microwave background (CMB) temperature, $T_{\rm CMB} = 2.725$ K (Mather et al. 1999; Fixsen 2009).

We obtain atmospheric state information from NASA's Modern-Era Retrospective analysis for Research and Applications version 2 (MERRA-2) database, which assimilates past measurements into a general circulation model to produce an estimate of the daily meteorological history of Earth's atmosphere dating back to 1980 (Rienecker et al. 2011; Molod et al. 2015; Gelaro et al. 2017). Among the quantities available in the MERRA-2 database are the temperature (T), specific humidity (q), mass mixing ratio of liquid water ($w_{\rm LWP}$), mass mixing ratio of ice water ($w_{\rm IWP}$), mass mixing ratio of ozone (O_3; w_{O_3}), and wind speed in the eastward and northward directions, all as a function of the pressure coordinate (P). Each of these quantities is regridded from native model coordinates onto latitude (every 0.°5), longitude (every 0.°625), pressure altitude (on up to 42 standard levels), and time (every 3 hr UTC). An example set of atmospheric quantities is shown in Figure 1.

[4] https://github.com/Smithsonian/ngehtsim

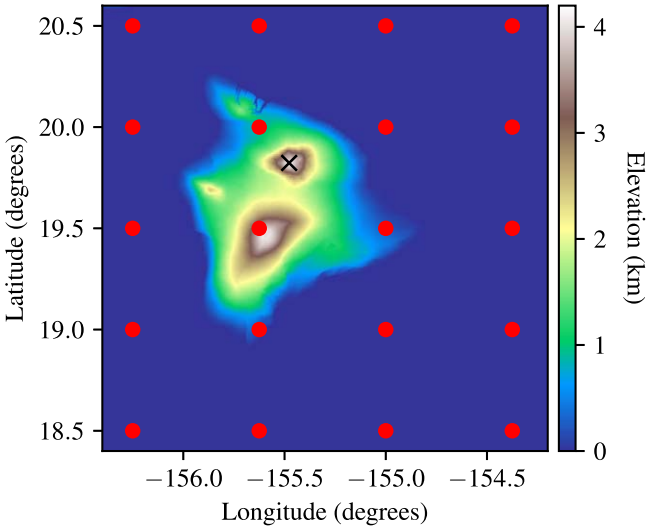

Figure 2. Topographical map of the island of Hawaii. The map is colored by elevation, and the overlaid red circles indicate the locations of the MERRA-2 grid points. The black cross marks the summit of Maunakea, which is the location of the submillimeter observing facilities JCMT and SMA. The MERRA-2 database provides only a few grid points covering the entire island, necessitating interpolation to estimate the atmospheric information above a specific telescope site (see Section 2.2).

The *am* code requires mixing ratios of H_2O and O_3 to be specified in terms of volume rather than mass. The H_2O mass mixing ratio w_{m,H_2O} is related to the specific humidity q by

$$w_{m,H_2O} = \frac{q}{1-q}. \quad (1)$$

To convert from the mass mixing ratio (w_{m,H_2O}) to the volume mixing ratio (w_{H_2O}), we multiply by the ratio of the relative molecular masses of air and water,

$$w_{H_2O} = 1.6078\, w_{m,H_2O}. \quad (2)$$

We apply a similar conversion to the O_3 mass mixing ratio provided in the MERRA-2 database, for which the conversion factor is 0.6034.

The liquid water path (LWP) and ice water path (IWP) are provided by MERRA-2 as mass mixing ratios (w) in each pressure layer, but *am* requires column densities (S). We convert from the former to the latter for each atmospheric layer using

$$S = \frac{w\Delta P}{g}, \quad (3)$$

where ΔP is the pressure difference between the upper and lower boundaries of the atmospheric layer and g is the standard acceleration of gravity on the surface of the Earth.

The *am* software also requires a choice of frequency resolution ($\Delta\nu$) and frequency range (ν_{min}, ν_{max}) over which to compute optical depths and brightness temperatures. Unless otherwise specified, we use values of $\nu_{min} = 0$ THz, $\nu_{max} = 2$ THz, and $\Delta\nu = 1$ GHz for all computations in this paper (see Appendix A).

2.2. Interpolation Scheme

The MERRA-2 data are supplied on a coarse grid in latitude and longitude, with individual grid cells measuring several tens of kilometers on a side. This cell size is much larger than the size of a typical mountain or other site on which a telescope might be located (see Figure 2), so we interpolate the MERRA-2 values when determining the atmospheric properties for a particular site.

For each site, we first identify the four MERRA-2 grid points that enclose it. All atmospheric quantities at each of these four locations are linearly interpolated in elevation onto a log-uniform grid of 100 atmospheric layers that span an elevation range [z_{site}, 70 km], where z_{site} is the elevation of the site itself and 70 km is chosen because it is roughly equal to the maximum elevation modeled by MERRA-2. The values of the elevation-dependent quantities in each layer are then bilinearly interpolated from the four surrounding grid point locations to the location of the site itself.

2.3. Weather Tabulation

Using the interpolated atmospheric state information from the MERRA-2 database as inputs to *am*, we have tabulated a variety of "weather parameters" for more than 80 sites that host existing or near-future radio or (sub)millimeter facilities around the globe. A partial list of sites is provided in Appendix E, and the complete list can be accessed from within `ngehtsim`. For each of these sites, we have tabulated the following weather parameters.

1. The ground-level air pressure (P), which we determine from the values recorded in the MERRA-2 database by interpolating to the location and elevation of the site as described in Section 2.2.
2. The ground-level air temperature (T_{air}), which we similarly determine from the MERRA-2 data after appropriate interpolation.
3. The ground-level wind speed (v_{wind}), which we determine as the quadrature sum of the eastward and northward wind speeds recorded in the MERRA-2 database after interpolating each to the location and elevation of the site.
4. The zenith precipitable water vapor (PWV), which is computed within *am* as an integral over the total water vapor column above the site.
5. The zenith atmospheric optical depth (τ_z) as a function of frequency, which is computed within *am* and recorded in `ngehtsim` on a frequency range that spans [0, 2] THz with 1 GHz spacing. To minimize the data volume, we use a principal component analysis (PCA) decomposition to compress the optical depth spectra stored in `ngehtsim`; our specific compression scheme is detailed in Appendix C.
6. The zenith atmospheric brightness temperature ($T_{b,z}$) as a function of frequency, which is also computed within *am* and is recorded and compressed in an analogous manner to the optical depth.

The MERRA-2 database provides atmospheric state information every 3 hr, but we average each of the above weather parameters on a per-day basis for the purposes of tabulation within `ngehtsim` (see Appendix B). These weather parameters have been calculated for all dates from 2012 January 1 up to 2023 January 1, and all are available as precomputed data tables within the `ngehtsim` package. An example time series of some of the weather parameters that can be accessed within `ngehtsim` is shown in Figure 3.

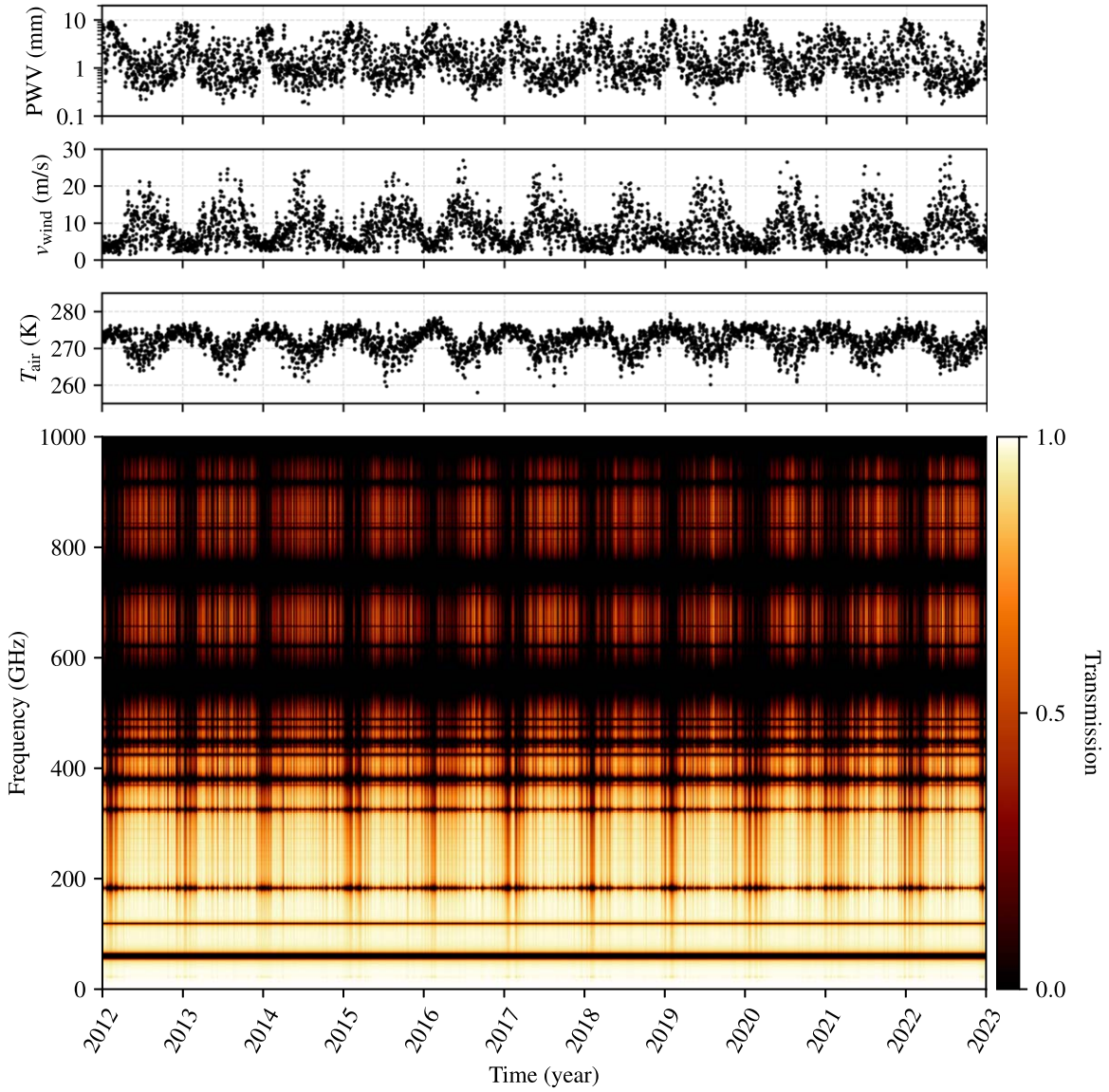

Figure 3. Example weather information tabulated in `ngehtsim`, shown for the ALMA site. The top panel shows the zenith PWV vs. time, the second panel shows the ground-level wind speed ($v_{\rm wind}$) vs. time, the third panel shows the ground-level air temperature ($T_{\rm air}$) vs. time, and the bottom panel shows the zenith atmospheric transmission ($e^{-\tau_z}$) as a function of both time and frequency.

3. Simulating Interferometric Data

The weather parameters tabulated within `ngehtsim` are used to determine telescope sensitivities during synthetic data generation. In this section, we detail how `ngehtsim` operates.

3.1. Initial Data Generation

Given a source model and a choice of array configuration, `ngehtsim` uses the `ehtim` library (Chael et al. 2016, 2018, 2023) to generate (u, v) coverage corresponding to a synthetic observation. We start by determining the values of the "Stokes visibilities" at each (u, v) point, which are initially set equal to the Fourier transform of the source model per (Thompson et al. 2017)

$$\tilde{I}(u, v) = \iint I(x, y) e^{2\pi i (ux+vy)} dxdy. \quad (4)$$

Here, I is the source model Stokes I brightness as a function of location (x, y) in the image plane and $\tilde{I}$ represents the Stokes I visibilities. An expression analogous to Equation (4) is also used to determine the initial Stokes Q, U, and V visibilities from the corresponding source model brightness maps. These Stokes visibilities are then converted to a circular correlation product representation via

$$\begin{pmatrix} V_{RR} \\ V_{RL} \\ V_{LR} \\ V_{LL} \end{pmatrix} = \begin{pmatrix} \tilde{I} + \tilde{V} \\ \tilde{Q} + i\tilde{U} \\ \tilde{Q} - i\tilde{U} \\ \tilde{I} - \tilde{V} \end{pmatrix}. \quad (5)$$

Currently, `ngehtsim` only produces data in a circular polarization basis, which is appropriate for most existing VLBI arrays. We assume that all visibilities have had absolute flux density calibration applied, such that both the measurements and their uncertainties can be expressed in physical units (e.g., Jy) rather than dimensionless correlation coefficients and

signal-to-noise ratios (SNRs). Gaussian random systematic errors are optionally applied to amplitude calibration.

3.2. Baseline Sensitivity

The sensitivity of the baseline comprised of stations i and j is characterized by a thermal noise level, σ_{ij}, determined by the radiometer equation and can be expressed as

$$\sigma_{ij} = \frac{1}{\eta_q}\sqrt{\frac{\mathrm{SEFD}_i^* \mathrm{SEFD}_j^*}{2\Delta\nu\Delta t}}. \quad (6)$$

Here, $\Delta\nu$ is the frequency bandwidth over which the measurement is being integrated for a single correlation product, Δt is the corresponding integration time,

$$\mathrm{SEFD}^* = \frac{2kT_{\mathrm{sys}}}{\eta_{\mathrm{ff}}\eta_w A_{\mathrm{eff}}} e^{\tau} \quad (7)$$

is the opacity-corrected "system equivalent flux density" (SEFD) for a station with system temperature T_{sys} and effective collecting area A_{eff}, k is the Boltzmann constant, τ is the line-of-sight atmospheric optical depth, η_{ff} is the forward efficiency of the antenna (controlling the degree of spillover; see, e.g., Mangum 2002), η_w is an efficiency factor associated with the wind buffeting the telescope, and η_q is an efficiency factor associated with digitization of the signal. Throughout this paper, we assume $\eta_q = 0.88$, appropriate for 2 bit quantization (Thompson et al. 2017). The thermal noise level given by Equation (6) is assumed to be the same for all four correlation products on a single baseline.

3.2.1. System Temperature

For each site, the system temperature is given by

$$T_{\mathrm{sys}} = [T_{\mathrm{rx}} + \eta_{\mathrm{ff}} T_{b,\mathrm{inc}} + (1 - \eta_{\mathrm{ff}}) T_{\mathrm{gnd}}](1 + r), \quad (8)$$

where T_{rx} is the receiver temperature, $T_{b,\mathrm{inc}}$ is the brightness temperature of the radiation incident on the dish, T_{gnd} is the ground temperature, and r is the sideband separation ratio (defined such that a perfectly sideband-separating receiver has $r = 0$ and a perfect double-sideband receiver has $r = 1$). Receiver temperatures differ from site to site and across frequencies, so `ngehtsim` includes some default values but also permits users to specify their own receiver temperatures. We set $T_{\mathrm{gnd}} = T_{\mathrm{air}}$ from the MERRA-2 database. An accurate determination of η_{ff} would require an elevation-dependent integral over the antenna beam pattern for each telescope (see, e.g., Rusch & Potter 1970), but for source elevations above $\sim 20°$, a typical amount of spillover contributes to the system temperature at the $\sim$several percent level (e.g., Potter 1973; Greve et al. 1998; Kramer et al. 2013; Mangum 2017). For the simulations in this paper, we assume a value of $\eta_{\mathrm{ff}} = 0.95$ for all antennas.

The incident brightness temperature $T_{b,\mathrm{inc}}$ contains contributions from the atmosphere, the CMB, and the source itself, and it is given by

$$T_{b,\mathrm{inc}} = T_{\mathrm{atm}}(1 - e^{-\tau}) + (T_{\mathrm{CMB}} + T_{\mathrm{source}})e^{-\tau}. \quad (9)$$

Here, T_{atm} is the effective atmospheric temperature,

$$T_{\mathrm{source}} = \frac{F_{\mathrm{tot}} A_{\mathrm{eff}}}{2k} \quad (10)$$

is the brightness temperature of the source, and F_{tot} is the total flux density of the source. We use a plane-parallel atmosphere approximation to obtain τ from the zenith optical depth τ_z via

$$\tau = \frac{\tau_z}{\sin(\theta_{\mathrm{el}})}, \quad (11)$$

where θ_{el} is the elevation angle of the observed source. τ_z is computed using *am* as described in Section 2.

Because the atmosphere does not have a single temperature, *am* instead computes a zenith atmospheric brightness temperature ($T_{b,z}$) that integrates over contributions from the full column of atmosphere above a site. To include an elevation dependence, we first determine an effective atmospheric temperature T_{atm} using

$$T_{\mathrm{atm}} = \frac{T_{b,z} - T_{\mathrm{CMB}} e^{-\tau_z}}{1 - e^{-\tau_z}}. \quad (12)$$

The effective atmospheric temperature is then appropriately scaled for nonzenith elevations when computing the system temperature (see Equation (9)).

3.2.2. Effective Area

The effective collecting area A_{eff} of a single-dish site is given by

$$A_{\mathrm{eff}} = \frac{\pi D^2 \eta_{\mathrm{ap}}}{4}, \quad (13)$$

where η_{ap} is the aperture efficiency and D is the dish diameter. For phased-array sites, we use an effective total diameter of

$$D = \sqrt{\frac{4}{\pi}\sum_j A_j}, \quad (14)$$

where A_j is the geometric area of the jth dish in the array and the sum is taken over all dishes in the array.

The aperture efficiency is determined by Ruze's law (Ruze 1952, 1966),

$$\eta_{\mathrm{ap}} = \exp\left[-\left(\frac{4\pi\sqrt{\sigma_{\mathrm{rms}}^2 + \sigma_{\mathrm{off}}^2}}{\lambda}\right)^2\right], \quad (15)$$

where σ_{rms} is the rms surface accuracy of the dish, σ_{off} is the typical focus offset in equivalent units of surface accuracy, and λ is the observing wavelength. Effective dish diameters and rms surface accuracies for existing and near-future sites whose weather information is tabulated in `ngehtsim` are provided in Appendix E. Throughout this paper, we assume $\sigma_{\mathrm{off}} = 10\,\mu$m, which is larger than the magnitude of defocus measured for some dishes (e.g., the Atacama Large Millimeter/submillimeter Array, ALMA; see Mangum et al. 2006) but still subdominant to the surface accuracy limitations for all antennas simulated within `ngehtsim`.

3.2.3. Sensitivity Degradation from Wind

High wind speeds can cause issues with telescope pointing, and intermittent changes in wind speed can rock a dish back and forth, decreasing its average sensitivity. We use the wind speeds tabulated from the MERRA-2 database to derive a

phenomenological efficiency factor, η_w, associated with these wind-related sensitivity losses.

We use a logistic function to capture the wind efficiency as a function of wind speed $v_{\rm wind}$,

$$\eta_w = 1 - \frac{1}{1 + \exp\left[-\frac{w}{2}\left(\frac{v_{\rm wind}}{2(v_s - v_d)} - 1\right)\right]}. \quad (16)$$

Here, v_d and v_s set the wind speeds within which substantial degradation occurs, such that for $v_{\rm wind} \lesssim v_d$, there is very little degradation, and for $v_{\rm wind} \gtrsim v_s$, the degradation is substantial; the quantity w sets the values of η_w at $v = v_d$ and $v = v_s$. Throughout this paper, we assume values of $v_d = 15\,{\rm m\,s^{-1}}$, $v_s = 25\,{\rm m\,s^{-1}}$, and $w = 10$. Given these settings, the wind efficiency takes on values of $\eta_w \approx 0.8$ when $v_{\rm wind} = v_d$ and $\eta_w \approx 0.2$ when $v_{\rm wind} = v_s$. While we expect that the actual degree of wind loading for an antenna will depend in detail on the antenna structure, observing frequency, and source elevation, the selected values are similar to specifications for telescopes such as ALMA (Greve & Mangum 2008) and the Greenland Telescope (GLT; Raffin et al. 2014).

3.3. Visibility Detection Scheme

Given a known source flux density (Section 3.1) and sensitivity (Section 3.2) for each baseline, `ngehtsim` uses a multistep visibility detection scheme that seeks to emulate the process of fringe-finding. As is evident in Equation (6), a baseline can, in principle, achieve arbitrary sensitivities by simply increasing the integration time Δt. However, rapid visibility phase fluctuations induced by changes in the atmospheric water vapor content over each site prevent coherent integration of visibilities for periods of time that are comparable to or longer than the atmospheric coherence timescale (i.e., the timescale over which the phase variance is equal to 1 rad), which is typically a few tens of seconds for millimeter-wavelength observations. The primary question that drives visibility detectability is thus whether the source can be detected with sufficient sensitivity and within a sufficiently short integration time, such that these rapid phase variations can be tracked and removed via calibration. Appendix G provides a more detailed discussion of the statistical character of these phase fluctuations and how baseline sensitivity and integration time impact our ability to track them.

The visibility detection scheme used in `ngehtsim` is based on SNR considerations, where we define the SNR (ρ) to be

$$\rho \equiv \frac{1}{\sqrt{2}\,\sigma}\left(\frac{|V_{RR} + V_{LL}|}{2}\right), \quad (17)$$

as appropriate for the Stokes I signal. Here, σ is the thermal noise (see Equation (6)) appropriate for this baseline at the observing time and frequency of interest. Given this definition for ρ, the detection algorithm proceeds as follows.

1. For each baseline, we first assess whether the SNR is sufficient to track phases on that baseline. Following Appendix G.1, we consider a "strong" baseline to be one that achieves $\rho \geqslant \rho_{\rm thresh}$ within an integration time of Δt. The visibilities on all strong baselines are considered to be detected.
2. If simultaneous multifrequency observations are being simulated, then frequency phase transfer (FPT) can be used to assist in visibility detection (see Appendix G.2). For each baseline, if the SNR at the reference frequency is at least $R\rho_{\rm thresh}$ (where R is the frequency ratio between the target and reference frequencies) within an integration time of Δt, then we consider that baseline to be "strong," and the visibility on that baseline is considered to be detected.
3. Following the approach developed in Blackburn et al. (2019), we partition the strong baselines into groups of mutually connected stations. All baselines between stations within a single such "fringe group" are considered to be detectable. Baselines that connect two stations contained in different fringe groups remain undetected.

Throughout this paper, we assume a threshold SNR value of $\rho_{\rm thresh} = 5$ and an integration time equal to one-third of the coherence time;[5] atmospheric coherence times are assumed to be (90, 30, 20, 10) s for observing frequencies of (86, 230, 345, 690) GHz. While we expect that coherence times should generically vary with telescope location and local weather conditions, and that they should also evolve with time throughout the duration of a single observation, the values selected here are approximately representative of the atmospheric conditions above millimeter-wavelength sites such as those participating in EHT observations (Event Horizon Telescope Collaboration et al. 2019b; see also Appendix G).

If the visibility on a baseline is detected, then we assume that all four correlation products on that baseline can be coherently integrated for arbitrarily long periods of time. Even so, we note that some of the "detections" resulting from the above procedure can still end up having arbitrarily low SNR; such visibilities may be more appropriately treated as consistent with nondetection at the level of the achieved final sensitivity.

4. Example Observations

In this section, we provide several examples of synthetic data generated using `ngehtsim` for current and potential future high-frequency VLBI observations with the EHT. All of the simulations presented here use version 1.0.0 of the `ngehtsim` software.

4.1. EHT 2017 Observations of M87*

The first EHT observing campaign from which images of M87* and Sgr A* were produced took place in 2017 April (Event Horizon Telescope Collaboration et al. 2019c). Calibrated data for both targets are publicly available online,[6] and telescope metadata are also available.[7] In this section, we compare an M87* data set from this observing campaign to corresponding data simulated using `ngehtsim`.

4.1.1. Array and Observation Characteristics

To mimic the real EHT observations, we use the settings specified in Table 1 to define the structure of the observing track. We aim to simulate the 2017 April 6 observation of M87* at the "low-band" observing frequency of 227.1 GHz; this observing track began at roughly 1 UT, lasted for

[5] One-third of the coherence time is the integration time over which ∼90% of the visibility amplitude is recovered.
[6] https://eventhorizontelescope.org/for-astronomers/data
[7] https://github.com/eventhorizontelescope/2020-D02-01

Table 1
Simulation Parameters for EHT 2017

Parameter	Value(s)
Sites	ALMA, APEX, JCMT, LMT, PV, SMA, SMT
Target source	M87*
Frequency	227.1 GHz
Bandwidth	2 GHz
Date	2017 Apr 6
Starting time	1 UT
Track duration	7 hr

Note. Parameters determining the structure of the observing track for our simulation of the 2017 April 6 EHT observations of M87*.

approximately 7 hr, and utilized 2 GHz of bandwidth for fringe-finding. We simulate the atmospheric conditions at every site using the procedure described in Section 2, starting with the MERRA-2 data for the specific 2017 April 6 date. The assumed receiver properties for each participating telescope are detailed in Appendix D, and the dish properties are provided in Appendix E.

Though `ngehtsim` contains information about the diameter of each telescope in the EHT array, not all dishes were able to use their full collecting area during the 2017 EHT observing campaign. As detailed in Event Horizon Telescope Collaboration et al. (2019b), the ALMA array observed with only 37 dishes (corresponding to an effective dish diameter of ∼73 m), and the Large Millimeter Telescope Alfonso Serrano (LMT) was operating with an effective diameter of only 32.5 m.[8] We thus override the default dish sizes for these stations in our simulation. Furthermore, some sites suffered from unmodeled sensitivity losses that are captured as "multiplicative mitigation factors" in Event Horizon Telescope Collaboration et al. (2019c); these factors inflate the system temperature in a manner similar to the sideband separation ratio. For our simulation, we follow Event Horizon Telescope Collaboration et al. (2019c) and increase the PV system temperature by a factor of 3.663 and the Submillimeter Array (SMA) system temperature by a factor of 1.4.

For the source structure, we use a geometric model that captures both the gross features observed in the M87* image (Event Horizon Telescope Collaboration et al. 2019d) and the finer-scale features expected from theory (Johnson et al. 2020); a detailed description of the source structure model is provided in Appendix F.

4.1.2. Simulation Results and Comparison with Real Data

Figure 4 shows the results of the `ngehtsim` simulation. The left panel compares the (u, v) coverage obtained from `ngehtsim` (in black) with that from the actual EHT observations (in red). The two sets of coverage are qualitatively similar, with the most notable differences being that some tracks appear to persist for longer in the synthetic data than they do in the real data. These tracks correspond to baselines containing the Submillimeter Telescope (SMT) station, which lost several scans at the beginning of the 2017 April 6 observing track (Event Horizon Telescope Collaboration et al. 2019c). The technical issues that resulted in these dropped scans are not simulated by `ngehtsim`, which thus over-predicts the amount of data on baselines containing the SMT.

The right panels of Figure 4 compare the simulated SEFDs of each telescope (in black) with the a priori estimates (in red) contained in the EHT metadata. Gross trends in the SEFDs at all telescopes are captured well by the simulation, with systematic deviations typically at the ∼10% level. Short-lived deviations are evident in the ALMA and SMA SEFDs, which exhibit large spikes in the measurements. These SEFD spikes are associated with momentary losses of phasing efficiency, as both of these sites join EHT observations as phased arrays; phasing efficiency is not simulated by `ngehtsim`, so it underpredicts the SEFDs during periods of poor array phasing. More systematic offsets are seen for a few stations (ALMA, APEX, and—most severely—PV), which likely arise from mismatches between the simplified antenna models assumed within `ngehtsim` and the true performance of the antennas. However, we note that the final SEFDs after self-calibration can often differ from their a priori values by $\gg$10% in EHT data (see, e.g., Event Horizon Telescope Collaboration et al. 2019d), which substantially exceeds the differences between the reported SEFDs and those predicted by `ngehtsim`.

4.2. EHT Observations at 0.87 mm

Many of the EHT stations are equipped with receivers capable of observing at a wavelength of 0.87 mm, and the EHT already exercised this capability during test observations in 2018 October (A. W. Raymond et al. 2024, in preparation) and 2021 April (observing M87*) and as part of a science campaign in 2023 April (observing Sgr A*). As of the time of writing for this paper, none of the data from the 2021 or 2023 observations have yet been published or publicly released, but we can nevertheless use `ngehtsim` to simulate the expected data quality of these and future 0.87 mm observations with the EHT. We describe and present such simulations in this section.

4.2.1. 2021 EHT Observations of M87*

To simulate the 2021 EHT observations of M87* at 0.87 mm, we use the settings specified in the second column of Table 2. For the source structure, we use the same geometric model as in Section 4.1, which is detailed in Appendix F, and the assumed receiver and dish properties for each participating telescope are detailed in Appendices D and E, respectively. As in Section 4.1, we simulate atmospheric conditions at each site that are specific to the 2021 April 19 observing date.

The left panel of Figure 5 shows the (u, v) coverage predicted by `ngehtsim` (in orange) compared with the coverage that would be obtained by the same array observing with infinite sensitivity (in gray). The simulation predicts that of the 16 distinct baselines that could have been detected by an arbitrarily sensitive version of the array, only four baselines—ALMA-PV, ALMA-NOEMA, NOEMA-PV, and the "zero baseline" JCMT-SMA—are actually able to recover detections under the specified observing conditions.

4.2.2. 2023 EHT Observations of Sgr A*

To simulate the 2023 EHT observations of Sgr A* at 0.87 mm, we use the settings specified in the third column of Table 2. For the source structure, we use a similar geometric model as in Sections 4.1 and 4.2.1, but with parameters that have been chosen to mimic the observed horizon-scale Sgr A*

[8] At the time, only 32.5 m out of the final 50 m of the LMT dish surface had been paneled.

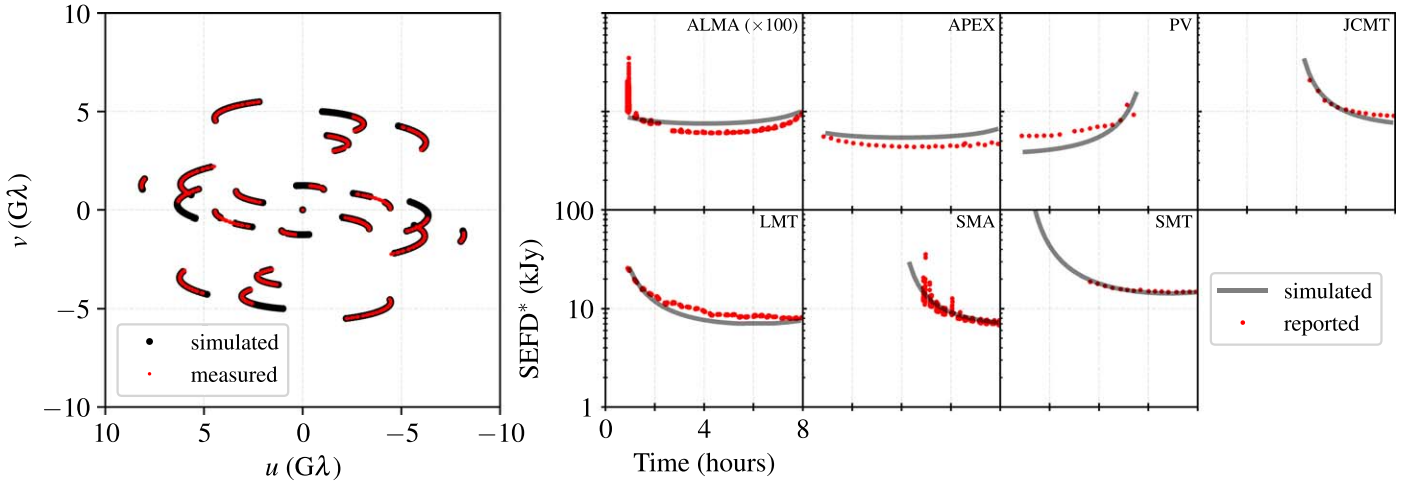

Figure 4. A comparison of the (u, v) coverage (left) and reported station SEFDs (right) between the real 2017 April 6 EHT data of M87* and a simulation of these data generated using `ngehtsim`; see Section 4.1 for simulation details. In all panels, the simulations are plotted in black, and the corresponding measurements or reported values are plotted in red. All of the SEFD panels on the right share common horizontal and vertical axis ranges, which are explicitly labeled in the LMT panel. Note that the SEFDs for the ALMA station have been increased by a factor of 100 to enable plotting on the same scale as used for the other stations.

Table 2
Simulation Parameters for EHT 0.87 mm Observations

Parameter	EHT 2021	EHT 2023	EHT Near-future
Sites	ALMA, GLT, JCMT, NOEMA, PV, SMA, SMT	ALMA, APEX, JCMT, SMA, SMT	ALMA, APEX, GLT, JCMT, LMT, NOEMA, PV, SMA, SMT, SPT
Target source	M87*	Sgr A*	M87*, Sgr A*
Frequency	337.6 GHz	337.6 GHz	337.6 GHz
Bandwidth	2 GHz	2 GHz	2 GHz
Date	2021 Apr 19	2023 Apr 15	Apr
Starting time	1 UT	2 UT	1 UT
Track duration	5 hr	13 hr	14 hr

Note. Parameters determining the structure of the observing tracks for our simulations of EHT observations at 0.87 mm observing wavelength.

structure and with the addition of interstellar scattering effects; Appendix F provides a detailed description of the source model. As in the previous sections, we use the receiver and dish properties detailed in Appendices D and E, respectively, and we simulate atmospheric conditions at each site that are specific to the 2023 April 15 observing date.

The third panel from the left panel in Figure 5 shows the (u, v)-coverage predicted by `ngehtsim` (in orange) compared with the coverage that would be obtained by the same array observing with infinite sensitivity (in gray). Though five stations took part in this observation, two pairs of them—ALMA-APEX (in Chile) and JCMT-SMA (in Hawaii)—are co-located and thus do not contribute geometrically unique baseline coverage. I.e., the array was effectively operating as a three-station one, plus the addition of a "zero baseline" comprised of the co-located sites. The simulation predicts that of the four distinct baselines that could have been detected by an arbitrarily sensitive version of the array, only two of them—Chile-SMT and the zero baseline—are actually able to recover detections under the specified observing conditions.

4.2.3. Near-future EHT Observations at 0.87 mm

Only a subset of the EHT array was able to participate in the 2021 and 2023 observations at 0.87 mm, limiting the (u, v)-coverage that could be achieved. In the near future, the EHT may carry out observations at 0.87 mm that feature a more complete array, including sites that do not currently have 0.87 mm receivers but which are planning to acquire them. We can use `ngehtsim` to simulate the expected performance of the array during such observations of M87* and Sgr A*. Our simulations use the settings specified in the fourth column of Table 2.

As in previous sections, we use the receiver and dish properties detailed in Appendices D and E, respectively. For the LMT and South Pole Telescope (SPT)—which are not currently equipped with 0.87 mm receivers—we assume specifications that match those of ALMA (i.e., a receiver temperature of $T_{\rm rx} = 75$ K and a sideband separation ratio of $r = 0.1$). Appendix F provides a detailed description of the source models for both M87* and Sgr A*. Because we do not know what the exact weather conditions will be for future observations, we instead simulate atmospheric conditions at each site by randomly selecting a past date and using the conditions from that date. For each observation, we run 100 simulations using different such samples of the historical global weather conditions in April, which permits us to evaluate the typical expected performance of the array.

The second and fourth panels from the left in Figure 5 show the (u, v) coverage predicted by `ngehtsim` (in orange) compared to the coverage that would be obtained by the same array observing with infinite sensitivity (in gray) for the M87* and Sgr A* simulations, respectively. The 100 weather instantiations are represented using the opacity of the plotted

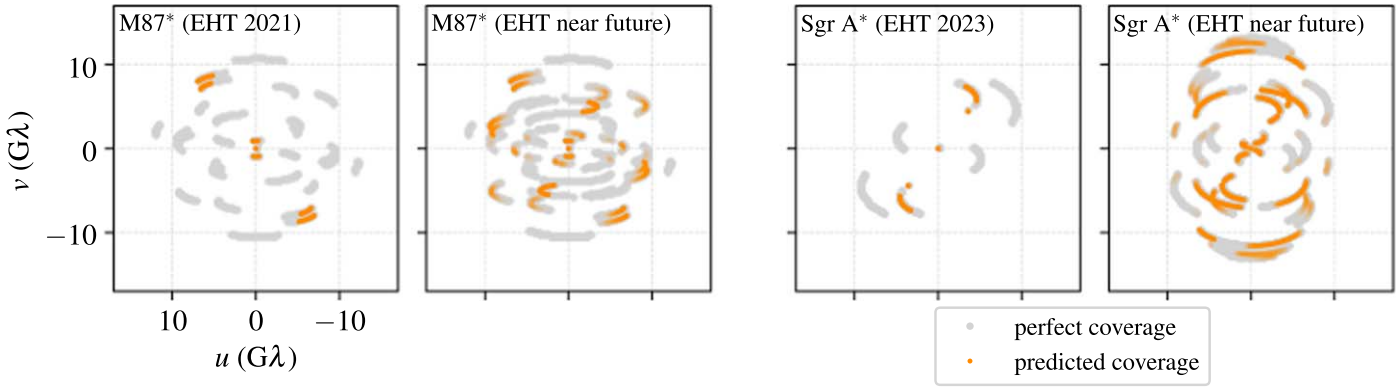

Figure 5. Simulated (u, v) coverage for past and near-future EHT observations at an observing wavelength of 0.87 mm; see Section 4.2 for simulation details. The leftmost panel shows the coverage predicted for an EHT observation of M87* carried out on 2021 April 19, and the second panel shows the coverage predicted for a near-future version of the EHT in which the LMT and APEX telescopes are also able to join the M87* observation at 0.87 mm. The third panel shows the coverage predicted for an EHT observation of Sgr A* carried out on 2023 April 15, and the rightmost panel shows the coverage predicted for a near-future version of the EHT in which the LMT, NOEMA, PV, and SPT telescopes are also able to join the Sgr A* observation at 0.87 mm. In all panels, gray points indicate visibilities that would have been detected if the array were observing with infinite sensitivity, and orange points indicate visibilities that `ngehtsim` predicts should be detected given the finite sensitivity of the real array. For the first and third panels from the left, we assume observing conditions appropriate for the specific dates 2021 April 19 and 2023 April 15, respectively. For the second and fourth panels from the left, we simulate 100 different instantiations of April weather conditions, and the opacity of each plotted point is proportional to how frequently it is detected. All panels share the same horizontal and vertical axis ranges, which are explicitly labeled in the left panel.

orange points, such that visibilities that are detected 100% of the time are fully opaque and visibilities that are detected 0% of the time are fully transparent (visibilities that are detected some fraction of the time are plotted with the corresponding fractional opacity). For both the M87* and Sgr A* observations, we see that the increased site participation noticeably improves the (u, v) coverage. However, it remains the case—particularly for M87*—that a substantial fraction of the baselines do not achieve detections.

For M87*, only a fraction 0.23 ± 0.08 of all baselines are detected, where we report the median and one standard deviation from the 100 weather instantiations; when considering only the geometrically unique baselines (i.e., consolidating redundant baselines such as ALMA-SMT and APEX-SMT), the detection fraction is 0.17 ± 0.07. The corresponding fractions for Sgr A* are 0.40 ± 0.08 for all baselines and 0.36 ± 0.11 for the geometrically unique baselines. Compared to analogous EHT observations at 1.3 mm observing wavelength—which are predicted to achieve typical detection fractions of >0.97 for both sources and both baseline groupings—the 0.87 mm observations suffer from a high fractional loss of detections.

4.3. Multifrequency Observations with a Next-generation EHT

As shown in the previous section, 0.87 mm observations carried out by the current and near-future EHT array are expected to achieve detection rates of no more than ∼50%. A key limitation driving this low detection fraction is the requirement for baselines to achieve sufficient sensitivity to track atmospheric phase variations within a fraction of the short (∼20 s) coherence timescale at 0.87 mm. A promising avenue toward realizing longer integration times is the FPT technique, whereby atmospheric phases tracked at some "reference" frequency—typically a lower frequency, where the dimensionless baseline lengths are shorter and the array more sensitive—can be transferred to simultaneous observations made at a "target" frequency (see, e.g., Rioja & Dodson 2020). As described in Section 3.3 (see also Appendix G.2), `ngehtsim` can simulate observations carried out using the FPT technique. In this section, we demonstrate the impact that FPT could have on 0.87 mm EHT observations of M87* and Sgr A*.

A number of EHT sites are planning to implement triband observing capabilities as part of a next-generation EHT upgrade (Doeleman et al. 2023), with a complement of receivers covering the 86 GHz (3 mm), 230 GHz (1.3 mm), and 345 GHz (0.87 mm) bands. Our simulations in this section adhere to the expected multifrequency capabilities following these upgrades; for the simulations of M87* and Sgr A*, we use the settings specified in the second and third columns of Table 3, respectively. For the M87* simulations, we assume that FPT will be carried out using the 3 mm band as the reference frequency, while for Sgr A*, we assume that the 1.3 mm band will be the reference frequency (to avoid the substantial effects of interstellar scattering at 3 mm). We continue to use the dish specifications provided in Appendix E, and we assume the 1.3 and 0.87 mm receiver specifications detailed in Appendix D (except for the LMT and SPT at 0.87 mm, for which we assume specifications that match those of ALMA, as in Section 4.2.3). For all sites observing with a 3 mm receiver band, we assume ALMA-like specifications, corresponding to a receiver temperature of $T_{\rm rx} = 40$ K and a sideband separation ratio of $r = 0.03$ (Claude et al. 2008). Note that although the upgrades specified in Doeleman et al. (2023) include increased bandwidths alongside the multifrequency capabilities, we continue to use 2 GHz bandwidths for the simulations in this section so as to isolate the impact of FPT and enable more direct comparisons with the results from prior sections (for analogous simulations that use wider bandwidths, see Sections 4.4.2 and 4.4.3). We also continue to use the source models described in Appendix F for both M87* and Sgr A*.

As in Section 4.2.3, we run 100 simulations for both M87* and Sgr A*, using different samples of the historical global weather conditions in April. Figure 6 shows the resulting (u, v) coverage predicted by `ngehtsim` (in orange) compared with the coverage that would be obtained by the same array observing with infinite sensitivity (in gray). For both the M87* and Sgr A* observations, we see that the addition of FPT noticeably improves the (u, v) coverage relative to the corresponding panels of Figure 5. For M87*, a fraction 0.55 ± 0.06 of all

Table 3
Simulation Parameters for Multifrequency EHT Observations

Parameter	M87* Observations	Sgr A* Observations
Sites	ALMA, APEX, GLT, JCMT, LMT, NOEMA, PV, SMA, SMT	ALMA, APEX, JCMT, LMT, NOEMA, PV, SMA, SMT, SPT
Target source	M87*	Sgr A*
Frequency	86 GHz, 345 GHz	230 GHz, 345 GHz
Bandwidth	2 GHz	2 GHz
Date	Apr	Apr
Starting time	1 UT	1 UT
Track duration	14 hr	14 hr
Dual-band sites	APEX, GLT, JCMT, LMT, SMT	APEX, JCMT, LMT, SMT, SPT
Single-band sites	ALMA, NOEMA, PV, SMA	ALMA, NOEMA, PV, SMA

Note. Parameters determining the structure of the observing tracks for our simulations of a future version of the EHT that observes at 0.87 mm using FPT from either 3 mm or 1.3 mm. The listed dual-band sites are assumed to observe at both specified frequencies, while the single-band sites are assumed to observe only at the higher frequency.

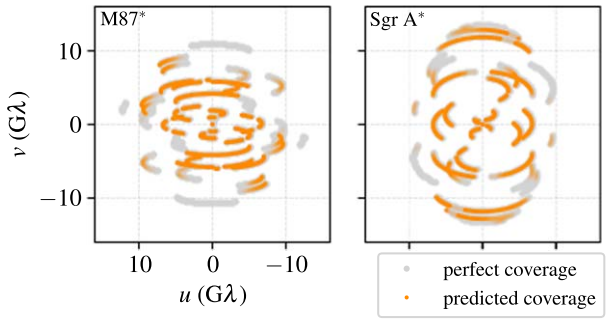

Figure 6. Simulated (u, v) coverage for a future version of the EHT observing at a wavelength of 0.87 mm and utilizing the FPT technique; see Section 4.3 for simulation details. The expected typical coverage achieved for observations of M87* is shown on the left, and the corresponding coverage achieved for observations of Sgr A* is shown on the right. The plotting style is analogous to that in Figure 5, with the opacity of each orange point corresponding to how frequently the corresponding visibility is detected.

baselines are detected, and a fraction 0.58 ± 0.06 of geometrically unique baselines are detected. The corresponding fractions for Sgr A* are 0.55 ± 0.06 for all baselines and 0.54 ± 0.08 for the geometrically unique baselines.

4.4. VLBI at Very High Frequencies

Though VLBI has not yet been carried out at wavelengths shorter than 0.87 mm, there are a number of atmospheric windows—such as those around 0.65 mm (460 GHz), 0.43 mm (690 GHz), and 0.34 mm (875 GHz)—that are accessible to high-elevation facilities (e.g., ALMA) and could seemingly permit VLBI observations. Not many (sub)millimeter facilities are currently equipped with appropriate receivers for observing at these higher frequencies, but it would, in principle, be possible to outfit them appropriately, and so we can nevertheless use `ngehtsim` to explore the prospects for VLBI at these frequencies.

4.4.1. Single-baseline Sensitivity

Figure 7 shows the thermal noise level achievable on three specific baselines—ALMA-GLTS,[9] ALMA-JCMT, and ALMA-SPT—as a function of observing frequency. Each of these baselines connects two stations that can experience exceptionally dry atmospheric conditions, and for each baseline, we have simulated the noise levels during the time of year expected to minimize the baseline thermal noise. We have also fixed $\eta_w = 1$ (see Equation (7)), equivalent to assuming negligible wind at all sites. These baselines are thus meant to represent the "best case" for high-frequency VLBI detection prospects using current or near-future facilities.

We simulate the ALMA-GLTS baseline observing M87* at 3 UT in April, corresponding to a source elevation of ∼54° at ALMA and ∼28°.5 at GLTS. We simulate the ALMA-JCMT baseline observing 3C 279 at 5 UT in May, corresponding to a source elevation of ∼42° at ALMA and ∼42° at JCMT. We simulate the ALMA-SPT baseline observing Sgr A* at 0 UT in August, corresponding to a source elevation of ∼79° at ALMA and ∼29° at SPT. For each of these simulations, we have assumed that both participating stations are equipped with an ALMA-like receiver suite whose specifications are listed in Table 4. The sensitivity curves in Figure 7 are shown for two different choices of bandwidth and integration time: (1) a bandwidth of $\Delta\nu = 2$ GHz and an integration time of $\Delta t = t_c$ (i.e., similar to the values that are most appropriate for current EHT observations) is shown in blue, and (2) a bandwidth of $\Delta\nu = 16$ GHz and an integration time of $\Delta t = 10$ minutes (i.e., similar to the values that might be relevant for a next-generation EHT employing the FPT technique) is shown in red. As in Sections 4.2.3 and 4.3, we sample 100 instantiations of the atmospheric conditions for each simulation, using different samples of the historical global weather conditions for the appropriate month; the corresponding range of baseline performance is indicated by the shaded region around each sensitivity curve in Figure 7.

For single-baseline measurements and assuming a circularly symmetric Gaussian source structure, we can associate a minimum detectable brightness temperature with the thermal noise limit using (see Lobanov 2015)

$$T_{b,\min} = \frac{\pi e \sigma_b b^2}{2k} \approx (3.1 \times 10^{11}\ \mathrm{K}) \left(\frac{\sigma_b}{1\ \mathrm{Jy}}\right) \left(\frac{b}{10^4\ \mathrm{km}}\right)^2, \quad (18)$$

where σ_b is the thermal noise level on the baseline, b is the projected baseline length, k is the Boltzmann constant, and e is the mathematical constant corresponding to the base of the natural

[9] The GLTS site is located at the summit of the Greenland ice sheet, with a latitude of 72°.580, a longitude of −38°.449, and an elevation of 3230 m. The GLT plans to relocate to the summit site, which has substantially drier atmospheric conditions than the current site (Matsushita et al. 2017). For these simulations, we thus retain the dish specifications provided in Appendix E but use the GLTS rather than the GLT site.

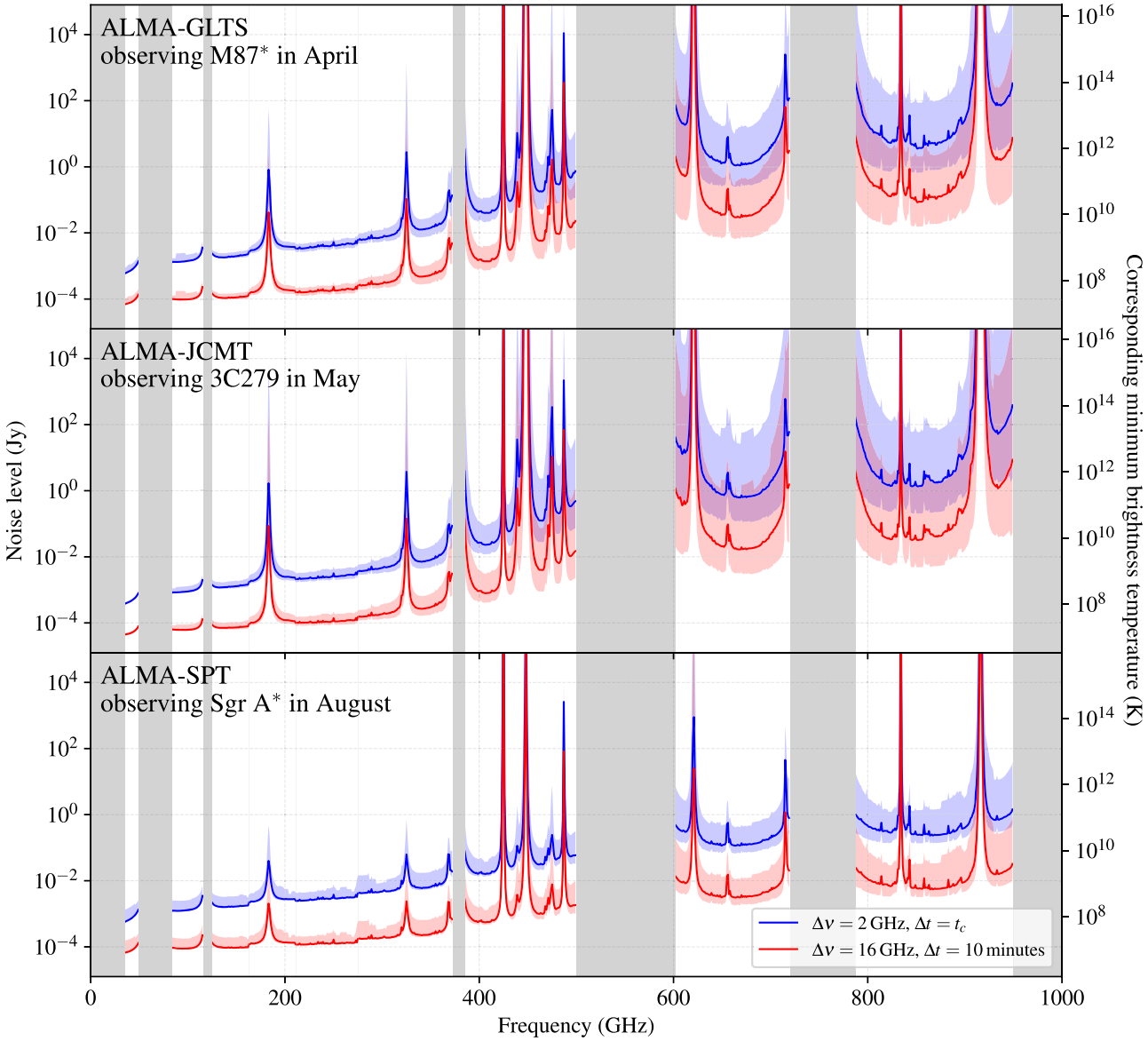

Figure 7. Thermal noise level achievable on three different baselines as a function of observing frequency; see Section 4.4.1 for simulation details. Each of these baselines has been selected because it connects two sites with exceptionally dry observing conditions, and we have selected the times of year and local observing times to optimize the quality of the weather for each of these simulations. Blue curves indicate performance expectations for capabilities that are comparable to those currently used by the EHT, while red curves indicate performance expectations for capabilities that substantially exceed those of current arrays but are similar to the planned capabilities of a next-generation EHT (Doeleman et al. 2023). In all cases, the central line shows the median rms thermal noise achieved from 100 instantiations of weather conditions appropriate for the specified month, and the lighter shaded region brackets the 90th percentile interval (i.e., spanning the 5th–95th percentile values). The darker gray vertical shaded regions indicate spectral ranges not currently covered by ALMA receiver bands. Large spikes in the rms noise level correspond to strong atmospheric lines (see, e.g., Figure 9).

logarithm. The minimum brightness temperature is indicated by the right-hand vertical axis for each of the panels in Figure 7.

It is evident from Figure 7 that the noise level rises rapidly toward higher observing frequencies. At the frequencies and capabilities of interest for current and near-future EHT observations—i.e., observing frequencies up to ∼345 GHz, bandwidths of ∼2 GHz, and integration times limited by the coherence time—the baseline thermal noise levels are typically below ∼20 mJy. At higher frequencies (e.g., corresponding to ALMA Band 9 and Band 10) and assuming the same capabilities, baseline thermal noise levels never get better than ∼100 mJy, with typical values being ∼1–10 Jy for ALMA-GLTS and ALMA-JCMT and ∼150–300 mJy for ALMA-SPT. When assuming capabilities that are more appropriate for a next-generation EHT—i.e., bandwidths of ∼16 GHz and integration times of ∼10 minutes—the expected baseline sensitivity improves by ∼1–2 orders of magnitude, reaching as low as ∼10 mJy for ALMA-GLTS and ALMA-JCMT and ∼2–3 mJy for ALMA-SPT in the highest observing bands.

4.4.2. Full-array VLBI of M87* and Sgr A*

The example baseline noise levels described in the previous section indicate that long-baseline observations at high observing frequencies could, in principle, achieve astrophysically relevant sensitivities, given the wide bandwidths and long integration times that are expected to be accessible to a next-generation EHT (and assuming that the sites are appropriately outfitted with the necessary receivers). However, the

Table 4
ALMA Receiver Properties

Band	Frequency (GHz)	T_{rx} (K)	r	References
Band 1	35–50	25	0.1	Huang et al. (2018)
Band 3	84–116	40	0.03	Claude et al. (2008)
Band 4	125–163	40	0.1	Asayama et al. (2008)
Band 5	163–211	55	0.1	Billade et al. (2012)
Band 6	211–275	40	0.01	Kerr et al. (2004)
Band 7	275–373	75	0.1	Mahieu et al. (2012)
Band 8	385–500	150	0.1	Sekimoto et al. (2008)
Band 9	602–720	100	1	Baryshev et al. (2008)
Band 10	787–950	100	1	Fujii et al. (2013)

Note. Receiver properties for the ALMA receiver suite, which are assumed for the simulations carried out in Section 4.4. T_{rx} is the receiver temperature, and r is the sideband separation ratio (see Equation (8)).

simulations in Section 4.4.1 are carried out on a per-baseline level, with the time of year and source location in the sky selected to optimize the performance of each baseline individually. For observations carried out using a more complete array, such optimization is not possible. Furthermore, the simulations in Section 4.4.1 only compute the achievable baseline noise level, and they do not take into account the corresponding expected source flux density on each baseline (which is necessary to determine detectability, per Section 3.3). In this section, we carry out high-frequency VLBI simulations of a futuristic version of the EHT array that is fully equipped with an ALMA-like suite of receivers.

For the simulations in this section, we assume that the entire EHT array has been equipped with a receiver suite whose specifications are listed in Table 4. We simulate April observations of both M87* and Sgr A* at observing frequencies of 230, 345, 460, 690, and 875 GHz, assuming a bandwidth of 16 GHz and an integration time of 10 minutes for all simulations. As in Section 4.3, we assume that FPT will be carried out using the 3 mm band as the reference frequency for M87* simulations, while for Sgr A*, we assume that the 1.3 mm band will be the reference frequency. We continue to use the dish specifications provided in Appendix E and the source models described in Appendix F for both M87* and Sgr A*, with the amount of interstellar scattering applied to the Sgr A* model adjusted appropriately for each simulated observing frequency. As in previous sections, we sample 100 instantiations of the atmospheric conditions for each simulation using different samples of the historical global weather conditions for April.

Figure 8 shows the (u, v) coverage predicted by `ngehtsim` (in color) compared against the coverage that would be obtained if the EHT were observing with infinite sensitivity (in gray) at all five observing frequencies. The M87* simulations are shown in the left column, and the Sgr A* simulations are shown in the second column from the left. For the colored visibilities—i.e., those labeled as an "achieved detection" in the figure—we plot only those detections that achieve an SNR of $\geqslant 1$ within the 10 minute integration time. For both M87* and Sgr A* observations, we see that the 230 and 345 GHz observations consistently achieve a nearly ∼100% detection rate, while the detection fraction drops off considerably at the higher frequencies. The 460 GHz simulations typically achieve detection fractions on nonintrasite baselines of 0.23 ± 0.09 and 0.29 ± 0.10 for M87* and Sgr A*, respectively, with the SNR on some of these baselines regularly exceeding a value of 10. For 690 and 875 GHz observations, it is common to have only one or zero nonintrasite baselines detected. The SNR on nonintrasite baselines for M87* observations at 690 and 875 GHz does not exceed 3 and 2, respectively. For Sgr A* observations at 690 and 875 GHz, the ALMA-SPT baseline is by far the most frequently detected, achieving peak SNR values of ∼9 and ∼6, respectively.

4.4.3. Full-array VLBI of the Brightest Sources

In addition to the substantially increased atmospheric optical depths at higher observing frequencies, another limiting factor is the modest correlated flux densities of M87* and Sgr A* on the longest baselines. In our models, M87* and Sgr A* have long-baseline (∼30 Gλ) flux densities of ∼10 mJy and ∼20 mJy, respectively. Other sources observed with the EHT —including 3C 279 (Kim et al. 2020), Centaurus A (Janssen et al. 2021), J1924–2914 (Issaoun et al. 2022), and NRAO 530 (Jorstad et al. 2023)—exhibit flux densities between ∼100 and ∼500 mJy on ∼10 Gλ baselines. Furthermore, the brightness temperature maximum expected for synchrotron emission is $\sim 10^{12}$ K (Kellermann & Pauliny-Toth 1969), corresponding (per Equation (18)) to correlated flux densities between ∼1 and ∼10 Jy on the longest baselines.[10] The detection prospects for VLBI observations of such sources could thus be substantially better than for M87* or Sgr A*.

Using the same array setup as in Section 4.4.2, we simulate observations of a hypothetical object that has a point-source emission structure and is located at the near-equatorial position of the radio source 3C 279. The right two columns of Figure 8 show the resulting (u, v) coverages for these observations assuming (second column from the right) a flux density of 1 Jy and (rightmost column) a flux density of 10 Jy. We see that even for the maximally optimistic case of a 10 Jy point source, the detection fraction begins to drop noticeably for observing frequencies above 345 GHz. At the highest simulated observing frequency of 875 GHz, the detection fraction on nonintrasite baselines is 0.13 ± 0.06 and 0.27 ± 0.08 for the 1 Jy and 10 Jy point source, respectively.

5. Summary and Conclusions

In this paper, we present `ngehtsim`, a Python-based software package for generating realistic synthetic data appropriate for high-frequency VLBI observations. `ngehtsim` includes a database of historical atmospheric information, which is tabulated for several dozen existing radio and (sub) millimeter telescope sites using more than a decade of MERRA-2 atmospheric state data processed through the *am* radiative transfer code. Synthetic observations generated with `ngehtsim` combine the resulting atmospheric optical depth and brightness temperature information with telescope and receiver specifications to determine baseline sensitivities across the array, from which a heuristic algorithm that emulates both single- and multifrequency fringe-finding techniques determines whether individual visibilities are detected.

[10] We note that there are fewer than 200 compact sources in the Planck 857 GHz catalog with flux densities above 1 Jy (Planck Collaboration et al. 2016), where "compact" for Planck means smaller than its roughly 4.′5 beam. Of these sources, none have spectral indices ($S_\nu \propto \nu^\alpha$) smaller than $\alpha \approx 0.8$, indicating that the population is likely to be dominated by dusty galaxies rather than synchrotron sources.

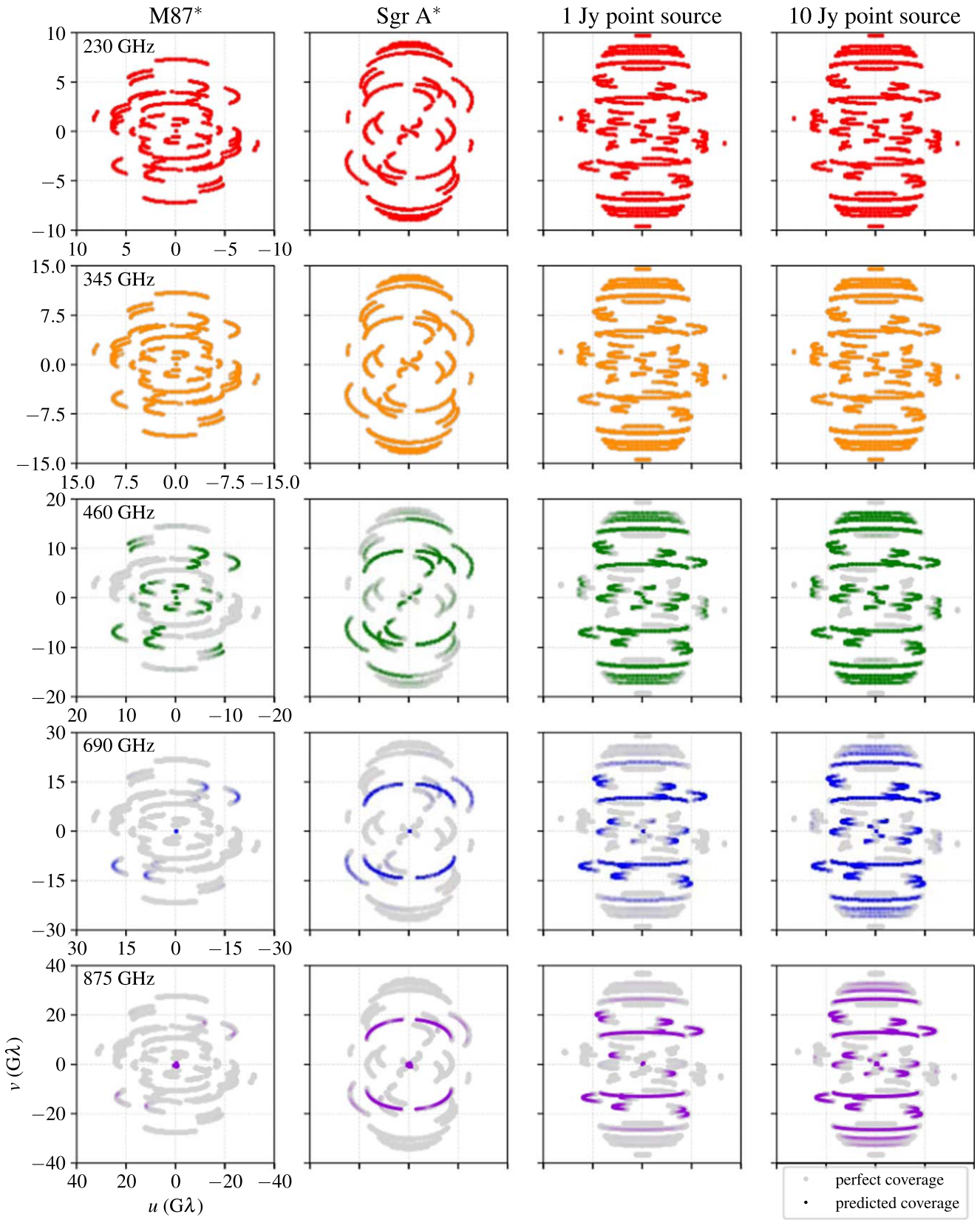

Figure 8. Simulated (u, v)-coverage plots for a hypothetical future EHT array capable of observing at multiple different frequencies (see Section 4.4). From left to right, the columns correspond to observations of M87*, Sgr A*, a 1 Jy point source, and a 10 Jy point source; the point sources are assumed to be located at the position of 3C 279. From top to bottom, the rows correspond to observing frequencies of 230, 345, 460, 690, and 875 GHz. The plotting style is analogous to that in Figure 5, with the opacity of each colored point corresponding to how frequently the corresponding visibility is detected. Each row of panels shares common horizontal and vertical axis ranges, which are explicitly labeled in the leftmost panel of the row.

We demonstrate the capabilities of `ngehtsim` by generating a series of example synthetic EHT observations of M87* and Sgr A*, two sources for which we have approximate knowledge of their structure on ∼microarcsecond scales. Synthetic observations generated by `ngehtsim` are able to reproduce well the 2017 EHT data that yielded the first published images of the M87* and Sgr A* black holes at an observing frequency of 230 GHz. Using `ngehtsim` to simulate past and future EHT observations at 345 GHz, we show that the 2021 and 2023 EHT observations of M87* and Sgr A*, respectively, will likely have low detection fractions and correspondingly poor (u, v) coverage (see first and third panels of Figure 5). Single-frequency image reconstructions will not be possible using these data sets. Near-future EHT observations of both M87* and Sgr A* at 345 GHz have the possibility to perform considerably better than prior observations, but they will continue to suffer from <50% detection fractions and much poorer (u, v) coverage than comparable observations at 230 GHz (see second and fourth panels of Figure 5).

The addition of simultaneous multifrequency observing capabilities to the EHT array can improve its detection prospects at 345 GHz through the use of the FPT calibration technique, yielding detection fractions that are consistently >50% (see Figure 6). Further improving the baseline sensitivity through, e.g., bandwidth upgrades across the array can bring the detection fraction at 345 GHz up to nearly 100%, matching the performance at 230 GHz (see Figure 8).

Anticipating the continuation of historical trends to push VLBI toward ever-higher observing frequencies, we use `ngehtsim` to simulate futuristic EHT-like observations at frequencies above 345 GHz. Given sufficiently wide bandwidths (∼16 GHz) and long integration times (∼10 minutes), baselines connecting exceptionally dry sites—such as ALMA, GLTS, JCMT, and SPT—can achieve astrophysically relevant sensitivities at observing frequencies that fall in atmospheric windows around, e.g., 460, 690, and 875 GHz (see Figure 7). However, array-wide observations of sources such as M87* and Sgr A* exhibit heavily degraded performance at these higher frequencies. Observations of M87* and Sgr A* with a futuristic EHT array that is appropriately outfitted to observe at 460 GHz could expect to regularly achieve multiple detections on long baselines, though with a detection fraction that does not exceed ∼30% (see Figure 8). Analogous observations at 690 and 875 GHz consistently see almost no detections at all beyond those on the single baseline ALMA-SPT, and even that baseline does not achieve SNRs above 10 in 10 minute integration times. High-frequency observations of continuum sources that are substantially brighter than either M87* or Sgr A* on long baselines (i.e., correlated flux densities $\gtrsim$1 Jy) are viable in principle, though detection fractions remain low ($\lesssim$30%), and it is unclear whether a population of sufficiently bright sources actually exists.

We note that one of the most important assumptions underpinning the simulations carried out in this paper is the value of the atmospheric coherence time at each observing frequency. For the simulations presented here, we have assumed a fixed set of coherence times, which have been selected to be characteristic of atmospheric conditions at millimeter-wavelength sites such as those participating in EHT observations. However, the specific values of the coherence times at each site are not known, and the quantitative details of the simulation predictions (e.g., detection fractions) depend—sometimes sensitively—on the assumed coherence times. The FPT calibration technique can mitigate the impact of an uncertain coherence time at the target frequency, but it still relies on knowledge of the coherence time at the reference frequency. While `ngehtsim` permits manual exploration of different coherence time assumptions, it does not automatically adjust the coherence time based on local weather conditions; future work is necessary to understand whether—and if so, how—local atmospheric state or other accessible physical information may be used to produce reasonable estimates of the coherence time.

We close by noting that although `ngehtsim` has been developed primarily for predicting current and next-generation EHT performance, it is a general-purpose tool that can readily simulate the performance of other existing or future arrays. As such, `ngehtsim` can be used for applications such as determining antenna placement during the design of future arrays, predicting array performance for observing proposals submitted to existing arrays, or supplying weather-informed telescope sensitivity estimates for initial flux density calibration of collected data.

Acknowledgments

We thank Avery Broderick, Dominic Chang, Roger Deane, Richard Dodson, Garret Fitzpatrick, Boris Georgiev, Linus Hamilton, Johnson Han, Aaron Oppenheimer, Nimesh Patel, Alex Raymond, María Rioja, Senkhosi Simelane, Ranjani Srinivasan, and Maciek Wielgus for various conversations and discussions that have been helpful throughout the course of this project. We also thank an anonymous referee for providing constructive comments that improved the quality of the paper.

Topographical information used in this paper has been obtained from the TessaDEM database (https://tessadem.com/), which is licensed under the Open Database License (ODbL) v1.0. This research has made use of the NASA/IPAC Extragalactic Database (NED), which is funded by the National Aeronautics and Space Administration and operated by the California Institute of Technology. This research has made use of the SIMBAD database, operated at CDS, Strasbourg, France.

Support for this work was provided by the NSF (AST-1935980, AST-2034306, and AST-2307887) and by the Gordon and Betty Moore Foundation through grant GBMF-10423. This work has been supported in part by the Black Hole Initiative at Harvard University, which is funded by grants from the John Templeton Foundation (grant No. 62286) and the Gordon and Betty Moore Foundation (grant GBMF-8273).

Software: am (Paine 2022), `ehtim` (Chael et al. 2016, 2018, 2023), `ehtplot` (Chan & Medeiros 2021), `matplotlib` (Hunter 2007), `netCDF4` (Whitaker et al. 2020), `ngehtsim` (Pesce et al. 2024), `numpy` (Harris et al. 2020), `paramsurvey` (https://github.com/wumpus/paramsurvey), `ray` (Moritz et al. 2017), stochastic optics (Johnson 2016), `scipy` (Virtanen et al. 2020).

Appendix A
Spectral Resolution

Figure 9 shows a comparison between an atmospheric transmission spectrum computed using a 1 GHz spectral resolution (in red) and a 1 MHz spectral resolution (in black). While the higher-resolution spectrum shows an

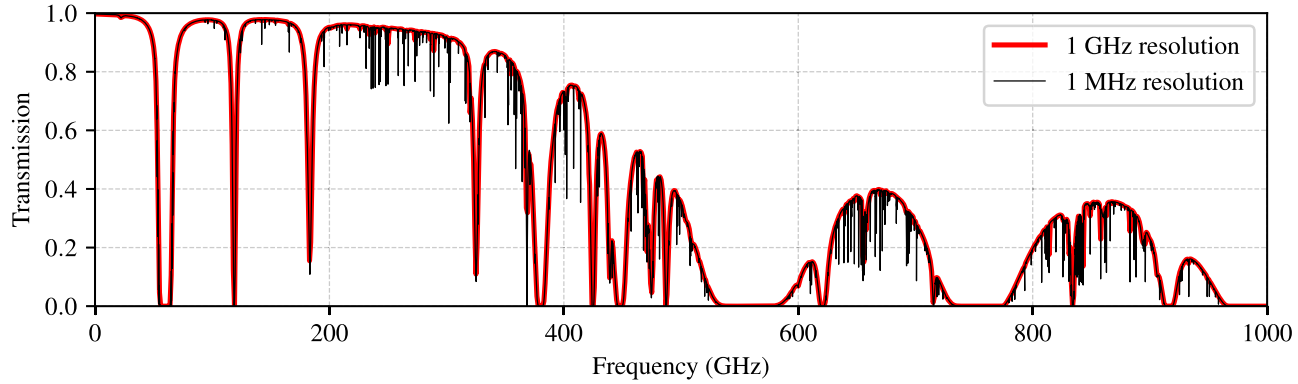

Figure 9. Comparison of the zenith atmospheric transmission spectrum over the ALMA site, computed using *am* set with two different spectral resolutions. The red spectrum is computed with 1 GHz spacing between spectral points, and the black spectrum is computed with 1 MHz spacing between spectral points. The atmospheric layer settings used to specify the *am* input for these spectra correspond to the 2022 April 15 MERRA-2 reanalysis at 0 UTC.

increased density of fine-scale absorption features, we see that the 1 GHz spectral resolution is sufficient to capture the dominant structures expected to be relevant for continuum observations.

Appendix B
Temporal Resolution

Figure 10 shows the optical depth versus time of day for each of the sites currently participating in the EHT array, assuming April observing conditions. The optical depth time series are plotted at the native 3 hr temporal resolution of the MERRA-2 database prior to carrying out the daily averaging that is used within `ngehtsim`. While some sites (e.g., LMT, NOEMA) exhibit clear differences between daytime and nighttime optical depths, many of the sites experience only modest variations. In all cases, the magnitude of the typical day-to-day variation—captured by the shaded regions in each panel—is comparable to or greater than the magnitude of the typical daytime-to-nighttime variation. Weather parameters that have been averaged on a per-day basis thus retain most of the interday variation that is relevant for generating realistic synthetic data using `ngehtsim`.

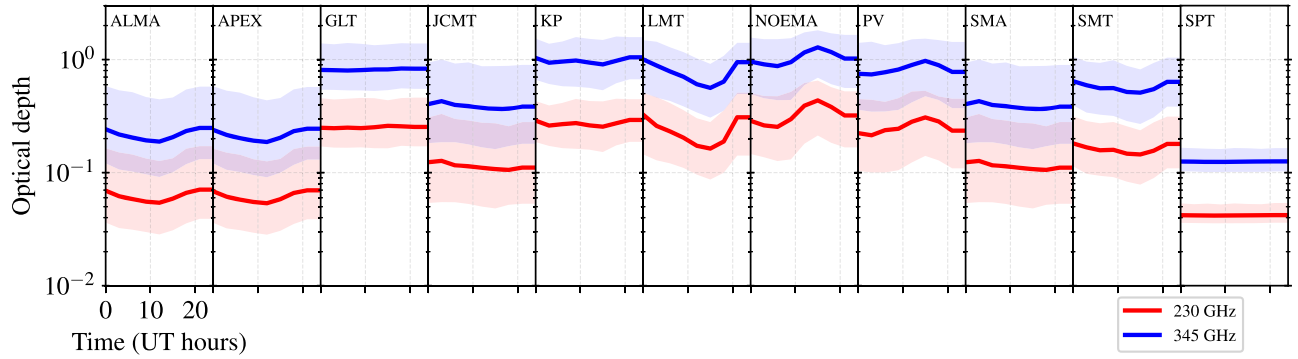

Figure 10. Optical depth vs. time of day at observing frequencies of 230 GHz (in red) and 345 GHz (in blue), assuming observing conditions appropriate for April at each of the stations currently participating in the EHT array. For both frequencies, the central line shows the median optical depth, and the shaded region brackets the 68th percentile interval (i.e., spanning the 16th–84th percentile values). All panels share the same horizontal and vertical axis ranges, which are explicitly labeled in the left panel.

Appendix C
PCA Decomposition of Atmospheric Spectra

Because we generate atmospheric optical depth and brightness temperature spectra with values spaced every 1 GHz from 0 to 2 THz, each of our spectra contains $N_\nu = 2001$ values. Given that `ngehtsim` requires access to the optical depth and brightness temperature spectra corresponding to every site at every day over a time range that spans more than a decade, we carry out PCA decomposition of these spectra to reduce the overall data volume.

Given N spectra $\boldsymbol{t}_i$, we compute a mean spectrum

$$\langle \boldsymbol{t} \rangle = \frac{1}{N} \sum_{i=1}^{N} \boldsymbol{t}_i \tag{C1}$$

and subtract it from each of the individual spectra to generate centered spectra,

$$\hat{\boldsymbol{t}}_i = \boldsymbol{t}_i - \langle \boldsymbol{t} \rangle. \tag{C2}$$

We then aggregate these centered spectra into an $N \times N_\nu$ matrix $\boldsymbol{X}$,

$$\boldsymbol{X} = \begin{pmatrix} \hat{\boldsymbol{t}}_1^\top \\ \hat{\boldsymbol{t}}_2^\top \\ \vdots \\ \hat{\boldsymbol{t}}_N^\top \end{pmatrix} = \begin{pmatrix} \hat{t}_1(\nu_1) & \hat{t}_1(\nu_2) & \dots & \hat{t}_1(\nu_{N_\nu}) \\ \hat{t}_2(\nu_1) & \hat{t}_2(\nu_2) & \dots & \hat{t}_2(\nu_{N_\nu}) \\ \vdots & \vdots & \ddots & \vdots \\ \hat{t}_N(\nu_1) & \hat{t}_N(\nu_2) & \dots & \hat{t}_N(\nu_{N_\nu}) \end{pmatrix}, \tag{C3}$$

whose associated $N_\nu \times N_\nu$ covariance matrix is given by

$$\boldsymbol{\Sigma} = \boldsymbol{X}^\top \boldsymbol{X}. \tag{C4}$$

The orthonormal set of eigenvectors $\boldsymbol{v}_j$ of $\boldsymbol{\Sigma}$ corresponds to the principal components, or "eigenspectra," of our decomposition. Each spectrum $\boldsymbol{t}_i$ can then be approximately reconstructed using an appropriate linear combination of eigenspectra,

$$\boldsymbol{t}_i \approx \langle \boldsymbol{t} \rangle + \sum_{j=1}^{n} A_{i,j} \boldsymbol{v}_j. \tag{C5}$$

The coefficients $A_{i,j}$ are obtained from projection of the centered spectra onto the eigenbasis,

$$A_{i,j} = \hat{\boldsymbol{t}}_i \cdot \boldsymbol{v}_j, \tag{C6}$$

and the number n of eigenspectra to use in the reconstruction depends on the desired trade-off between the fidelity of approximation and the degree of compression.

To ensure a high-fidelity approximation across many orders of magnitude in τ, we perform PCA on the logarithm of the optical depth; our decomposition of T_b uses the linear spectrum. We use $\sim$1.6 million full spectra—corresponding to every spatial and temporal point contained in the MERRA-2 database for 2022 April 15—to determine the PCA decomposition for both τ and T_b. We find that the first $n = 40$ principal components are typically sufficient to achieve a maximum residual of $\lesssim$1 K in T_b and $\lesssim 10^{-2}$ in each of the optical depth, log optical depth, and transmission. Recording only the coefficients corresponding to these components yields a storage savings of approximately a factor of 50.

Appendix D
Receiver Properties

Table 5 lists the telescope and receiver properties assumed for EHT stations in the simulations carried out in this paper.

Table 5
Receiver Properties for EHT Stations

Station	1.3 mm Receiver			0.87 mm Receiver			References
	Frequency (GHz)	T_{rx} (K)	r	Frequency (GHz)	T_{rx} (K)	r	
ALMA	211–275	40	0.01	275–373	75	0.1	Kerr et al. (2004); Mahieu et al. (2012)
APEX (2017)	211–275	90[a]	0.03	…	…	…	Vassilev et al. (2008)
APEX (post-2017)	196–281	85[b]	0.03	272–376	120	0.03	Meledin et al. (2022)
GLT	207–235	70	0.01	275–373	150	0.1	Hasegawa et al. (2017); Han et al. (2018)
JCMT (2017)	215–270	50	1.25	…	…	…	JCMT website[c]
JCMT (post-2017)	212–273	60	0.03	275–373	80	0.03	Mizuno et al. (2020)
KP	211–275	80[d]	0.03[d]	…	…	…	…
LMT (2017)	209–233	130[e]	1	…	…	…	EHTC et al. (2019c)
LMT (post-2017)	210–280	70	0.03[f]	…	…	…	Bustamante et al. (2023)
NOEMA	200–276	80	0.1	275–373	150	0.1	Chenu et al. (2016)
PV	200–267	60	0.03	260–360	85	0.03	Carter et al. (2012)
SMA	194–281	70	1	258–408	130	1	Wilner (1998)
SMT	205–280	80	0.03	325–370	150	1	SMT website[g]
SPT	212–230	40	0.03	…	…	…	Kim et al. (2018)

Notes. Receiver properties assumed for the simulations carried out in Sections 4.1–4.3. The APEX, JCMT, and LMT sites received upgrades to their equipment after the initial 2017 EHT observations, so there are two sets of receiver properties provided for each of these sites.
[a] The receiver temperature measured for the APEX-1 receiver during commissioning was ∼120 K (Vassilev et al. 2008), but receiver improvements over time reduced this value to ∼90 K by 2017 (see https://www.apex-telescope.org/heterodyne/shfi/het230/characteristics/index.php).
[b] See http://www.apex-telescope.org/ns/nflash/.
[c] See https://www.eaobservatory.org/jcmt/instrumentation/heterodyne/rxa/.
[d] Assumed to match SMT.
[e] The 2017 LMT receiver temperature has been estimated from the system temperature measurements in Event Horizon Telescope Collaboration et al. (2019c), assuming an atmospheric temperature of 273 K and optical depth of 0.2.
[f] See http://lmtgtm.org/ single-pixel-1mm-receiver/.
[g] See https://aro.as.arizona.edu/?q=facilities/uarizona-aro-submillimeter-telescope. Receiver temperatures for the SMT have been estimated from the provided system temperature measurements assuming an atmospheric temperature of 273 K and optical depth of 0.2.

Appendix E
Site Information

Table 6 lists the locations, elevations, effective dish diameters, and surface accuracies for a number of existing and near-future sites for which atmospheric information is available in `ngehtsim`.

Table 6
Information for Sites Available in `ngehtsim`

Site Code	Location	Latitude	Longitude	Elevation (m)	D (m)	$\sigma_{\rm rms}$ (μm)
ALMA	Atacama, Chile	−23.032	−67.755	5040	75	25
AMT	Gamsberg, Namibia	−23.339	16.229	2340	15	25
APEX	Atacama, Chile	−23.005	−67.759	5060	12	25
ATCA	New South Wales, Australia	−30.313	149.564	210	54	200
EFF	Cologne, Germany	50.525	6.884	390	100	550
GBT	West Virginia, US	38.434	−79.840	810	100	260
GLT	Pituffik Space Base, Greenland	76.535	−68.686	70	12	50
HAY	Massachusetts, US	42.624	−71.489	110	37	85
JCMT	Maunakea, Hawaii	19.823	−155.477	4070	15	24
KP	Arizona, US	31.953	−111.615	1930	12	16
KVNPC	Pyeongchang, South Korea	37.534	128.450	500	21	70
KVNTN	Tamna, South Korea	33.289	126.460	410	21	70
KVNUS	Ulsan, South Korea	35.546	129.249	130	21	70
KVNYS	Yonsei, South Korea	37.565	126.941	90	21	70
LLA	Salta, Argentina	−24.192	−66.475	4780	12	25
LMT	Sierra Negra, Mexico	18.986	−97.315	4620	50	80
MET	Uusimaa, Finland	60.218	24.393	50	13.7	100
NOB	Nagano Prefecture, Japan	35.944	138.472	1370	45	100
NOEMA	Plateau de Bure, France	44.634	5.907	2550	50	35
ONS	Halland County, Sweden	57.396	11.926	30	20	128
OVRO	California, US	37.231	−118.282	1210	10.4	40
PV	Sierra Nevada, Spain	37.066	−3.393	2860	30	55
SMA	Maunakea, Hawaii	19.824	−155.478	4070	15	20
SMT	Arizona, US	32.702	−109.891	3170	10	15
SPT	South Pole, Antarctica	−90.000	0.000	2820	10	25
VLA	New Mexico, US	34.079	−107.618	2120	130	420
VLBBR	Washington, US	48.131	−119.683	260	25	320
VLBFD	Texas, US	30.635	−103.945	1610	25	320
VLBHN	New Hampshire, US	42.934	−71.987	310	25	320
VLBKP	Arizona, US	31.956	−111.612	1920	25	320
VLBLA	New Mexico, US	35.775	−106.246	1970	25	320
VLBMK	Maunakea, Hawaii	19.802	−155.456	3730	25	320
VLBNL	Iowa, US	41.771	−91.574	240	25	320
VLBOV	California, US	37.232	−118.277	1210	25	320
VLBPT	New Mexico, US	34.301	−108.119	2370	25	320
VLBSC	St. Croix, US Virgin Islands	17.757	−64.584	10	25	320
YEB	Castilla-La Mancha, Spain	40.523	−3.088	920	40	150

Note. Location, elevation, effective dish diameter (D), and surface accuracy ($\sigma_{\rm rms}$) for existing and near-future sites available in `ngehtsim`.

Appendix F
Geometric Source Structure Models for M87* and Sgr A*

A key property determining the detectability of a source on interferometric baselines is the source's emission structure. For the simulations carried out in this paper, we use tailored geometric source structure models to mimic the horizon-scale appearances of M87* and Sgr A* at the (sub)millimeter wavelengths of interest. Our basic model building block is the so-called "m-ring" geometric model, introduced in Johnson et al. (2020) and used extensively in Event Horizon Telescope Collaboration et al. (2022d) to model the observed structure of Sgr A*. While purely phenomenological, the m-ring model has the benefit of capturing the gross features observed by the EHT that are present in the horizon-scale emission structure around M87* and Sgr A* using a small number of parameters.

An infinitesimally thin m-ring can be parameterized in terms of its total flux density S_0, its diameter D, an elongation parameter s, an orientation angle ψ, and a series of complex Fourier coefficients β_k that describe the azimuthal intensity distribution. In terms of these parameters, we can express the image intensity I in modified polar coordinates (r, ϕ) as

$$I_{\rm ring}(r, \phi) = \frac{S_0}{\pi D s}\delta\left(r - \frac{D}{2}\right)\sum_{k=-m}^{m}\beta_k e^{ik\phi}. \tag{F1}$$

Here, m is an integer that sets the order of the azimuthal expansion, $\beta_k = \beta_k^*$, for all k because the image has real-valued intensities, and we fix $\beta_0 = 1$ so that S_0 sets the total flux density. The modified polar coordinates are related to modified Cartesian coordinates (x', y') via

$$r^2 = x'^2 + y'^2$$
$$\tan(\phi) = \frac{y'}{x'}, \tag{F2}$$

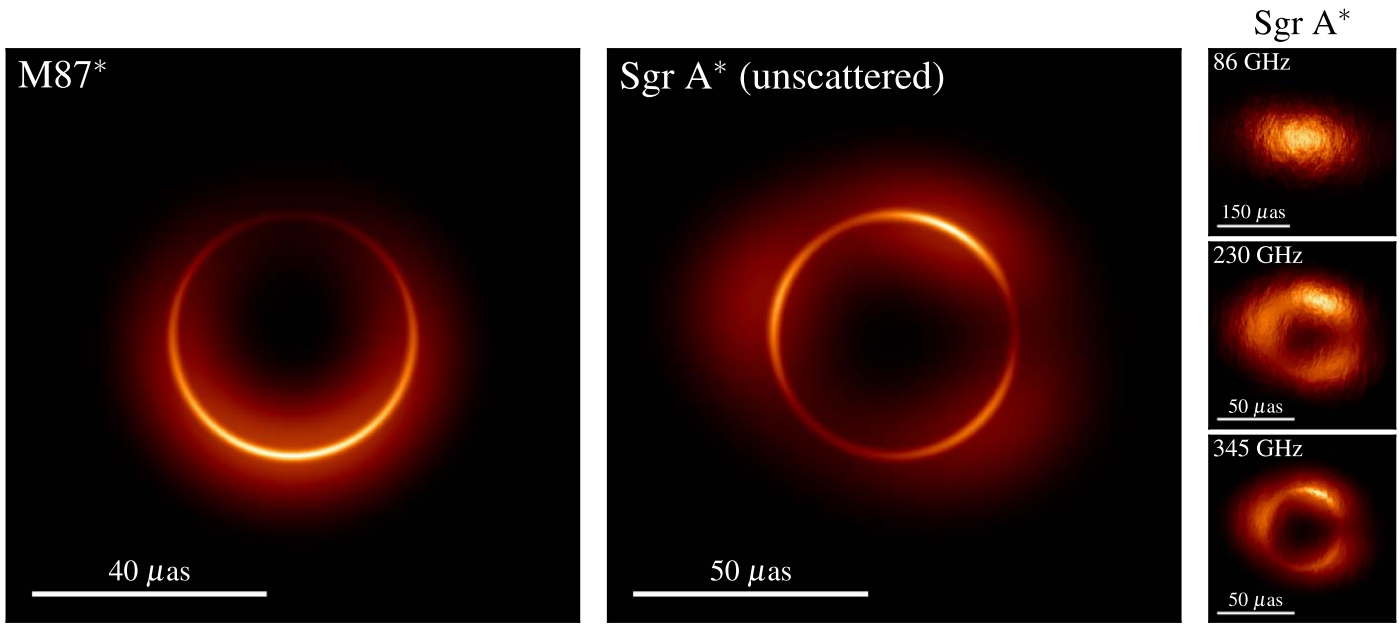

Figure 11. Source models of M87* (left panel) and Sgr A* (rightmost four panels) used for the simulations carried out in this paper. The source structure for M87* is assumed to be independent of frequency, while the Sgr A* source structure evolves substantially with frequency because of the effects of interstellar scattering. The second panel from the left shows the underlying unscattered Sgr A* source structure, which we assume to be independent of frequency. The three smaller panels on the right show the corresponding on-sky Sgr A* source structure after applying the effects of interstellar scattering at three different observing frequencies; from top to bottom, the three observing frequencies are 86, 230, and 345 GHz.

which in turn are related to the standard image-plane Cartesian coordinates (x, y) via the stretching transformation

$$\begin{pmatrix} x' \\ y' \end{pmatrix} = \begin{pmatrix} \cos^2(\psi) + \dfrac{\sin^2(\psi)}{s} & \cos(\psi)\sin(\psi)\left(\dfrac{1}{s} - 1\right) \\ \cos(\psi)\sin(\psi)\left(\dfrac{1}{s} - 1\right) & \dfrac{\cos^2(\psi)}{s} + \sin^2(\psi) \end{pmatrix} \times \begin{pmatrix} x \\ y \end{pmatrix}. \tag{F3}$$

To produce an m-ring with a finite thickness, we then convolve Equation (F1) with a circular Gaussian having FWHM α,

$$I_{\mathrm{m-ring}}(r, \phi) = \frac{4\ln(2)}{\pi\alpha^2} \exp\left(-\frac{4\ln(2) r^2}{\alpha^2}\right) * I_{\mathrm{ring}}(r, \phi). \tag{F4}$$

We use Equation (F4) to produce mock images of both M87* and Sgr A* for the simulations carried out in this paper.

We model M87* using a sum of two concentric m-rings. This model choice is intended to capture the expected structure corresponding to the first two images of the multiply lensed emission, with a thicker m-ring representing the direct emission and a thinner m-ring representing emission from the first-order lensed image or "photon ring" (Johnson et al. 2020). Both m-rings have order $m = 1$, corresponding to a single ~dipolar asymmetry in the otherwise ringlike emission structure (see Event Horizon Telescope Collaboration et al. 2019d, 2019f). We set the total flux density to be $S_0 = 0.6$ Jy, with 90% of the flux density in the direct emission and 10% of the flux density in the photon ring. The ring diameter is set to be $D = 42$ μas for both m-rings, and the ring width is $\alpha = 15$ μas for the direct emission and $\alpha = 1.5$ μas for the photon ring. The single Fourier coefficient is set to be $\beta_1 = -0.4$ for both m-rings. The left panel of Figure 11 shows the M87* image structure resulting from this model; for the simulations carried out in this paper, we assume that this source structure is independent of frequency.

We similarly model Sgr A* using a sum of two concentric m-rings. Both m-rings have order $m = 4$, permitting sufficient flexibility to capture the more complex azimuthal intensity structure observed toward Sgr A* (see Event Horizon Telescope Collaboration et al. 2022b, 2022c, 2022d; Wielgus et al. 2022). We set the total flux density to be $S_0 = 2.5$ Jy, again apportioned such that 90% of the flux density is in the direct emission and 10% of the flux density is in the photon ring. The ring diameter is set to be $D = 52$ μas for both m-rings, and the ring width is $\alpha = 20$ μas for the direct emission and $\alpha = 2$ μas for the photon ring. The four Fourier coefficients are set to be the same for both m-rings, taking on values of

$$\begin{aligned} \beta_1 &= 0.15, \\ \beta_2 &= 0.06\exp(-2.3\pi i), \\ \beta_3 &= 0.25\exp(0.5\pi i), \\ \beta_4 &= 0.13\exp(-1.4\pi i). \end{aligned}$$

The stretch parameter is set to be $s = 1.2$ for the direct emission and $s = 1$ for the photon ring, and the orientation parameter is $\psi = (\pi/2) - 0.2$ for both m-rings. We apply frequency-dependent interstellar scattering effects to the images using the "stochastic optics" package (Johnson 2016) as implemented within `ehtim`, which uses the scattering screen parameters measured by Johnson et al. (2018). The corresponding images of Sgr A* are shown in the right four panels of Figure 11; the large panel shows the unscattered image structure (which we assume to be the same at all frequencies), and the three smaller rightmost panels show the scattered images at observing frequencies of 86, 230, and 345 GHz.

Appendix G
Atmospheric Phase Variations

Variations in the amount of atmospheric water vapor cause corresponding variations in the index of refraction, which then serve as the primary source of rapid phase fluctuations at (sub) millimeter wavelengths (Thompson et al. 2017). The standard model for these phase fluctuations is that they can be described by a phase screen obeying the so-called "Taylor hypothesis" (Taylor 1938), which assumes that the turbulent structures giving rise to the refractive variations in the atmosphere are "frozen" over the observational timescales of interest. Typical practice is to describe the distribution of phase turbulence in terms of a "structure function" (e.g., Treuhaft & Lanyi 1987; Asaki et al. 2007; Natarajan et al. 2022),

$$D(r) = \langle [\phi(\boldsymbol{x} + \boldsymbol{r}) - \phi(\boldsymbol{x})]^2 \rangle, \tag{G1}$$

where $\boldsymbol{x}$ and $\boldsymbol{r}$ are transverse position vectors in the screen and the angle brackets denote an ensemble average. The structure function provides the mean squared phase difference between two locations on the screen separated by $\boldsymbol{r}$, and we have implicitly assumed isotropy by casting the structure function in terms of the magnitude of this separation, $r = |\boldsymbol{r}|$.

Given the frozen screen assumption, the spatial phase variations can be related to temporal phase variations through the transformation $r \rightarrow vt$, where $v \approx 10\,\mathrm{m\,s^{-1}}$ is the transverse velocity of the phase screen and t is time. For a wide range of spatial scales, the structure function is then well described by a power law in t (Kolmogorov 1941; Dravskikh & Finkelstein 1979; Coulman 1985),

$$D(t, \lambda) = \left(\frac{1\ \mathrm{mm}}{\lambda}\right)^2 \left(\frac{t}{t_{c,1\ \mathrm{mm}}}\right)^{\alpha}, \tag{G2}$$

where $t_{c,1\ \mathrm{mm}}$ is the coherence timescale on which the phase variance is equal to 1 rad at an observing wavelength of $\lambda = 1$ mm. The value of α depends on the relative size of the observing wavelength and the length scales governing the turbulent medium; for wavelengths shorter than the vertical extent of the turbulent layer ($\sim$1 km; Carilli & Holdaway 1999) but longer than the dissipative scale ($\sim$1 mm; Stotskii 1973), α takes on the value of $\sim 5/3$ appropriate for 3D Kolmogorov turbulence (Thompson et al. 2017). We will adopt the value $\alpha = 5/3$ for the remainder of this paper.

A typical 1 mm coherence timescale at a centimeter-wavelength site like the Very Large Array (VLA) is $t_{c,1\ \mathrm{mm}} \approx 10$ s (Beasley & Conway 1995), while for the millimeter-wavelength sites used in the EHT array, the coherence timescale can be longer by a factor of several (Event Horizon Telescope Collaboration et al. 2019b).

G.1. Phase Tracking: Sensitivity and Integration Time Considerations

Calibrating the phase measurements in interferometric observations requires being able to accurately track the phase fluctuations induced by geometric, instrumental, and atmospheric effects, which in turn requires a certain sensitivity to be achieved in the phase measurements. Regardless of the specific precision requirements for any particular experiment, given some fixed observing conditions, there will always be some integration time below which the SNR ρ is insufficient to provide the target precision. We would thus like to determine the integration time t_{int} that is necessary to achieve a desired threshold SNR ρ_{thresh} in our phase measurement. We assume that once this threshold SNR is achieved, the phases can be calibrated sufficiently well to integrate for arbitrarily long times, assuming that the source visibility is not evolving appreciably during the integration period (or that it can be modeled well).

Denoting the thermal phase noise on an integration time of t_0 by $\sigma_{\mathrm{th},0}$, the thermal phase noise $\sigma_{\mathrm{th}}(t_{\mathrm{int}})$ on an integration time t_{int} is given by

$$\sigma_{\mathrm{th}}(t_{\mathrm{int}}) = \sigma_{\mathrm{th},0}\left(\frac{t_0}{t_{\mathrm{int}}}\right)^{1/2}. \tag{G3}$$

Here, we note that the reference thermal noise $\sigma_{\mathrm{th},0}$ does not depend on any characteristics of the atmospheric turbulence; it is purely a description of the measurement sensitivity, which will typically be determined by properties such as the collecting areas of the telescopes, the level of receiver noise, the integrated frequency bandwidth, and the brightness of the observed source.

The existence of intrinsic phase fluctuations on all timescales means that any amount of averaging will miss some phase variations, primarily those associated with timescales shorter than the averaging time t_{int}. That is, there is an additional source of phase noise that arises during the averaging process itself, which is associated with the intrinsic evolution of the phase with time over the duration of the averaging period. For a signal with structure function given by Equation (G2), the residual phase variance $\sigma^2_{\mathrm{res},i}$ contributed by station i after boxcar averaging over an interval t_{int} is given by Blackburn et al. (2019),

$$\sigma^2_{\mathrm{res},i} = \frac{2^{-\alpha}(2 + \alpha - 2^{\alpha})}{(1 + \alpha)(2 + \alpha)}\left(\frac{t_{\mathrm{int}}}{t_{c,i}}\right)^{\alpha} \equiv K\left(\frac{t_{\mathrm{int}}}{t_{c,i}}\right)^{\alpha}, \tag{G4}$$

where $t_{c,i}$ is the coherence time at station i and K is a constant that depends only on α. For $\alpha = 5/3$, $K \approx 0.016$. It is convenient to define an effective coherence time t_c,

$$t_c \equiv \left(\frac{1}{t^{\alpha}_{c,i}} + \frac{1}{t^{\alpha}_{c,j}}\right)^{-1/\alpha}, \tag{G5}$$

such that

$$\sigma^2_{\mathrm{res},i} + \sigma^2_{\mathrm{res},j} = K\left(\frac{t_{\mathrm{int}}}{t_c}\right)^{\alpha}. \tag{G6}$$

The quantity t_c provides a notion of the coherence time for the baseline connecting stations i and j, rather than for each station individually. If $t_{c,i} = t_{c,j}$ and $\alpha = 5/3$, then the effective coherence time is shortened by a factor of $\sim$0.66 relative to that at either station.

The total phase noise σ_{tot} incurred after averaging on a timescale t_{int} will then be determined by a combination of the thermal (Equation (G3)) and residual (Equation (G6)) phase noises,

$$\sigma_{\mathrm{tot}}(t_{\mathrm{int}}) = \sqrt{\sigma^2_{\mathrm{th}} + \sigma^2_{\mathrm{res},i} + \sigma^2_{\mathrm{res},j}}. \tag{G7}$$

For stations that are geographically separated and thus observing through different atmospheric phase screens—as is

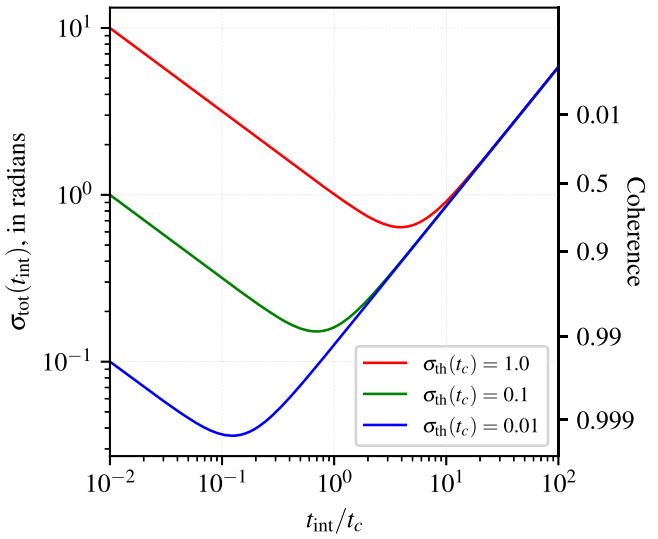

Figure 12. Total phase noise (Equation (G7)) as a function of integration time. Three different baseline sensitivity values—characterized by their thermal phase noise levels on a coherence time—are plotted as different colored lines and labeled accordingly. The right-hand vertical axis indicates the phase coherence corresponding to a particular total phase noise value, where the coherence is given by $\exp(-\sigma_{\rm tot}^2/2)$.

typically the case for VLBI—we expect $\sigma_{{\rm res},i}$ and $\sigma_{{\rm res},j}$ to be independent, such that their variances simply add in Equation (G7). Figure 12 shows $\sigma_{\rm tot}(t_{\rm int})$ for several different choices of baseline sensitivity.

Given fixed values of α, $\sigma_{{\rm th},0}$, t_0, and t_c, there is a value of $t_{\rm int}$ that minimizes $\sigma_{\rm tot}$. This minimum value of $\sigma_{\rm tot}$ is given by

$$\begin{aligned}\sigma_{\rm min} &= \sigma_{{\rm th},c}^{\alpha/(1+\alpha)}\sqrt{(\alpha^{1/(1+\alpha)} + \alpha^{-\alpha/(1+\alpha)})K^{1/(1+\alpha)}} \\ &\approx 0.64\sigma_{{\rm th},c}^{5/8},\end{aligned} \tag{G8}$$

where for convenience we have taken $t_0 = t_c$ and thus relabeled $\sigma_{{\rm th},0} \rightarrow \sigma_{{\rm th},c} = \sigma_{\rm th}(t_c)$, and in the second line, we have explicitly plugged in $\alpha = 5/3$. The corresponding integration time required to achieve $\sigma_{\rm min}$ is given by

$$\begin{aligned}\frac{t_{\rm max}}{t_c} &= \left(\frac{\sigma_{{\rm th},c}^2}{\alpha K}\right)^{1/(1+\alpha)} \\ &\approx 3.91\sigma_{{\rm th},c}^{3/4},\end{aligned} \tag{G9}$$

where in the second line we have again explicitly plugged in $\alpha = 5/3$. $t_{\rm max}$ represents the longest integration time that will typically be useful for a given value of $\sigma_{{\rm th},c}$; integrating for longer than $t_{\rm max}$ will result in increased total phase noise. If the minimum phase noise that a baseline can achieve never falls below some threshold value $\sigma_{\rm thresh}$, then the phase on that baseline cannot be accurately tracked, and the visibilities on that baseline are effectively undetected. The values of both $t_{\rm max}$ and $\sigma_{\rm min}$ are determined by the baseline sensitivity ($\sigma_{\rm th}$) and effective coherence time (t_c), as shown in Figure 12.

The rule of thumb we follow for the simulations in this paper is that the thermal SNR on a baseline must be at least $\rho_{\rm thresh} \geqslant 5$ on an integration time of $t_{\rm int} = t_c/3$ (see Section 3.3). Per Equation (G3), this condition corresponds to $\sigma_{{\rm th},c} \approx 0.12$ rad, which in turn implies that $\sigma_{\rm min} \approx 0.17$ rad (Equation (G8)) and $t_{\rm max} \approx 0.77 t_c$ (Equation (G9)); i.e., requiring that the thermal SNR be at least 5 on an integration time of $t_c/3$ is sufficient to ensure that the achievable total phase noise is better than ~0.2 rad. For comparison, typical SNR values for EHT observations of M87* are ~0.3–10 on non-ALMA baselines within a $t_c/3 \approx 10$ s integration time (Event Horizon Telescope Collaboration et al. 2019c); by our rule-of-thumb criterion, the visibility phases on these baselines cannot always be tracked without some alternative source of phase stabilization.

G.2. Phase Tracking: Multifrequency

The tropospheric phase fluctuations that dominate the atmospheric component of the phase variations at high radio frequencies are largely nondispersive, meaning that the magnitude of the phase variations increases linearly with frequency (see Equation (G2)). This behavior means that if the atmospheric phase variations can be tracked at one frequency, then they can then be used to calibrate concurrent measurements made at another frequency by scaling the phase solutions by the frequency ratio. This calibration technique—known as FPT (Rioja & Dodson 2020)—leverages the relative ease of observations at lower frequencies to bolster or even enable observations at higher frequencies.[11] FPT-based calibration provides a promising avenue for pushing millimeter VLBI to higher frequencies and fainter flux densities (e.g., Issaoun et al. 2023; Rioja et al. 2023), and it is emulated within `ngehtsim`.

Let us use ν_ℓ and ν_h to denote the low (reference) and high (target) frequencies, respectively. We will define

$$R = \frac{\nu_h}{\nu_\ell} = \left(\frac{t_{c,\ell}}{t_{c,h}}\right)^{\alpha/2} \tag{G10}$$

to be the frequency ratio. The transfer of phase from the reference frequency to the target frequency involves a multiplication by the frequency ratio R, which also inflates the noise in the phase measurement. The resulting additional phase noise transferred to the target frequency from the reference frequency is then given by

$$\sigma_{\rm FPT} = R\sqrt{\sigma_{{\rm th},\ell}^2 + \sigma_{{\rm res},\ell,1}^2 + \sigma_{{\rm res},\ell,2}^2}\,, \tag{G11}$$

where $\sigma_{{\rm th},\ell}$ is the thermal noise at the reference frequency and $\sigma_{{\rm res},\ell,i}$ is the residual phase noise at the reference frequency from station i.

Up to a constant scaling factor of R, the excess phase noise imparted during FPT (Equation (G11)) is the same as the total phase noise of the reference frequency phase signal (Equation (G7)). The optimal integration time $t_{\rm max}$ that minimizes $\sigma_{\rm FPT}$ will thus remain the same as in Equation (G9), while the effective noise in the transferred phase—i.e., ignoring the thermal noise at the target frequency itself—will be increased by a factor of R relative to that in Equation (G8). So to achieve any given threshold noise level $\sigma_{\rm thresh}$ in the phase transferred to the target frequency requires a factor of R lower phase noise at the reference frequency.

This scaling also means that FPT is only useful in practice—i.e., it will only provide improved phase tracking over that obtained through single-frequency observations—if the phase

[11] Note that FPT is not restricted to transferring phase from low frequencies to high frequencies; in principle, the phase could be tracked at the higher frequency and then transferred to the lower frequency. But in practice, it is almost always the case that the direction of most useful phase transfer goes from lower to higher frequency.

measurement at the reference frequency is sufficiently more sensitive than the phase measurement at the target frequency. The thresholding requirement is that the phase measurement at the reference frequency must satisfy $\sigma_{\mathrm{th},0,\ell} < \sigma_{\mathrm{th},0,h}/R$; i.e., the thermal phase noise at the reference frequency (within any given integration time) must be a factor of R smaller than the corresponding thermal phase noise at the target frequency. We expect that lower-frequency observations will typically be more sensitive than those at higher frequencies, both because characteristic system noises tend to increase with frequency and because sources tend to have higher correlated flux densities on shorter dimensionless baseline lengths. However, the answer to the question of whether any particular reference–target frequency pair is suitable for FPT will ultimately be both source- and telescope-dependent.

ORCID iDs

Dominic W. Pesce https://orcid.org/0000-0002-5278-9221
Lindy Blackburn https://orcid.org/0000-0002-9030-642X
Sara Issaoun https://orcid.org/0000-0002-5297-921X
Michael D. Johnson https://orcid.org/0000-0002-4120-3029
Greg Lindahl https://orcid.org/0000-0002-6100-4772
Iniyan Natarajan https://orcid.org/0000-0001-8242-4373
Scott N. Paine https://orcid.org/0000-0003-4622-5857
Daniel C. M. Palumbo https://orcid.org/0000-0002-7179-3816
Freek Roelofs https://orcid.org/0000-0001-5461-3687
Paul Tiede https://orcid.org/0000-0003-3826-5648

References

Asaki, Y., Sudou, H., Kono, Y., et al. 2007, PASJ, 59, 397
Asayama, S., Kawashima, S., Iwashita, H., et al. 2008, in Ninteenth Int. Symp. on Space Terahertz Technology, ed. W. Wild, 244, https://www.nrao.edu/meetings/isstt/papers/2008/2008244249.pdf
Bare, C., Clark, B. G., Kellermann, K. I., Cohen, M. H., & Jauncey, D. L. 1967, Sci, 157, 189
Baryshev, A. M., Mena, F. P., Adema, J., et al. 2008, Ninteenth Int. Symp. on Space Terahertz Technology, ed. W. Wild, 258, https://www.nrao.edu/meetings/isstt/papers/2008/2008258262.pdf
Beasley, A. J., & Conway, J. E. 1995, in ASP Conf. Ser. 82, Very Long Baseline Interferometry and the VLBA, ed. J. A. Zensus, P. J. Diamond, & P. J. Napier (San Francisco, CA: ASP), 327
Billade, B., Nystrom, O., Meledin, D., et al. 2012, ITTST, 2, 208
Blackburn, L., Chan, C.-k., Crew, G. B., et al. 2019, ApJ, 882, 23
Blecher, T., Deane, R., Bernardi, G., & Smirnov, O. 2017, MNRAS, 464, 143
Broten, N. W., Legg, T. H., Locke, J. L., et al. 1967, Sci, 156, 1592
Burke, B. F., Papa, D. C., Papadopoulos, G. D., et al. 1970, ApJL, 160, L63
Bustamante, S., Blackburn, L., Narayanan, G., Schloerb, F. P., & Hughes, D. 2023, Galax, 11, 2
Carilli, C. L., & Holdaway, M. A. 1999, RaSc, 34, 817
Carter, M., Lazareff, B., Maier, D., et al. 2012, A&A, 538, A89
Chael, A., Issaoun, S., Pesce, D. W., et al. 2023, ApJ, 945, 40
Chael, A. A., Johnson, M. D., Bouman, K. L., et al. 2018, ApJ, 857, 23
Chael, A. A., Johnson, M. D., Narayan, R., et al. 2016, ApJ, 829, 11
Chan, C.-k., & Medeiros, L., 2021 ehtplot: Plotting Functions for the Event Horizon Telescope, Astrophysics Source Code Library, ascl:2106.038
Chenu, J.-Y., Navarrini, A., Bortolotti, Y., et al. 2016, ITTST, 6, 223
Claude, S., Jiang, F., Niranjanan, P., et al. 2008, Proc. SPIE, 7020, 70201B
Coulman, C. E. 1985, ARA&A, 23, 19
Crew, G. B., Goddi, C., Matthews, L. D., et al. 2023, PASP, 135, 025002
Doeleman, S., Blackburn, L., Dexter, J., et al. 2019, BAAS, 51, 256
Doeleman, S. S., Barrett, J., Blackburn, L., et al. 2023, Galax, 11, 107
Doeleman, S. S., Weintroub, J., Rogers, A. E. E., et al. 2008, Natur, 455, 78
Dravskikh, A. F., & Finkelstein, A. M. 1979, Ap&SS, 60, 251
Event Horizon Telescope Collaboration, Akiyama, K., Alberdi, A., et al. 2019a, ApJL, 875, L1
Event Horizon Telescope Collaboration, Akiyama, K., Alberdi, A., et al. 2019b, ApJL, 875, L2
Event Horizon Telescope Collaboration, Akiyama, K., Alberdi, A., et al. 2019c, ApJL, 875, L3
Event Horizon Telescope Collaboration, Akiyama, K., Alberdi, A., et al. 2019d, ApJL, 875, L4
Event Horizon Telescope Collaboration, Akiyama, K., Alberdi, A., et al. 2019e, ApJL, 875, L5
Event Horizon Telescope Collaboration, Akiyama, K., Alberdi, A., et al. 2019f, ApJL, 875, L6
Event Horizon Telescope Collaboration, Akiyama, K., Alberdi, A., et al. 2022a, ApJL, 930, L12
Event Horizon Telescope Collaboration, Akiyama, K., Alberdi, A., et al. 2022b, ApJL, 930, L13
Event Horizon Telescope Collaboration, Akiyama, K., Alberdi, A., et al. 2022c, ApJL, 930, L14
Event Horizon Telescope Collaboration, Akiyama, K., Alberdi, A., et al. 2022d, ApJL, 930, L15
Event Horizon Telescope Collaboration, Akiyama, K., Alberdi, A., et al. 2022e, ApJL, 930, L16
Event Horizon Telescope Collaboration, Akiyama, K., Alberdi, A., et al. 2022f, ApJL, 930, L17
Event Horizon Telescope Collaboration, Akiyama, K., Alberdi, A., et al. 2023, ApJL, 957, L20
Event Horizon Telescope Collaboration, Akiyama, K., Algaba, J. C., et al. 2021a, ApJL, 910, L12
Event Horizon Telescope Collaboration, Akiyama, K., Algaba, J. C., et al. 2021b, ApJL, 910, L13
Fixsen, D. J. 2009, ApJ, 707, 916
Fujii, Y., Gonzalez, A., Kroug, M., et al. 2013, ITTST, 3, 39
Gelaro, R., McCarty, W., Suárez, M. J., et al. 2017, JCli, 30, 5419
Greve, A., Kramer, C., & Wild, W. 1998, A&AS, 133, 271
Greve, A., & Mangum, J. 2008, IAPM, 50, 66
Han, C.-C., Chen, M.-T., Huang, Y.-D., et al. 2018, Proc. SPIE, 10708, 1070835
Harris, C. R., Millman, K. J., van der Walt, S. J., et al. 2020, Natur, 585, 357
Hasegawa, Y., Asayama, S., Harada, R., et al. 2017, PASJ, 69, 91
Huang, Y.-D. T., Morata, O., Koch, P. M., et al. 2018, Proc. SPIE, 10708, 1070833
Hunter, J. D. 2007, CSE, 9, 90
Inoue, M., Algaba-Marcos, J. C., Asada, K., et al. 2014, RaSc, 49, 564
Issaoun, S., Pesce, D. W., Roelofs, F., et al. 2023, Galax, 11, 28
Issaoun, S., Wielgus, M., Jorstad, S., et al. 2022, ApJ, 934, 145
Janssen, M., Falcke, H., Kadler, M., et al. 2021, NatAs, 5, 1017
Janssen, M., Goddi, C., van Bemmel, I. M., et al. 2019, A&A, 626, A75
Johnson, M. D. 2016, ApJ, 833, 74
Johnson, M. D., Lupsasca, A., Strominger, A., et al. 2020, SciA, 6, eaaz1310
Johnson, M. D., Narayan, R., Psaltis, D., et al. 2018, ApJ, 865, 104
Jorstad, S., Wielgus, M., Lico, R., et al. 2023, ApJ, 943, 170
Kellermann, K. I., & Pauliny-Toth, I. I. K. 1969, ApJL, 155, L71
Kerr, A. R., Pan, S. K., Lauria, E. F., et al. 2004, Fifteenth Int. Symp. on Space Terahertz Technology, ed. G. Narayanan, 55
Kim, J., Marrone, D. P., Beaudoin, C., et al. 2018, Proc. SPIE, 10708, 107082S
Kim, J.-Y., Krichbaum, T. P., Broderick, A. E., et al. 2020, A&A, 640, A69
Kolmogorov, A. 1941, DoSSR, 30, 301
Kramer, C., Penalver, J., & Greve, A. 2013, Improvement of the IRAM 30m Telescope Beam Pattern, IRAM, https://cloud.iram.fr/index.php/s/4rDsGTRMesp3Wd6
Lobanov, A. 2015, A&A, 574, A84
Mahieu, S., Maier, D., Lazareff, B., et al. 2012, ITTST, 2, 29
Mangum, J. 2002, Load Calibration at Millimeter and Submillimeter Wavelengths ALMA Memo 434, NRAO, https://library.nrao.edu/public/memos/alma/memo434.pdf
Mangum, J. 2017, ALMA Sensitivity Metric for Science Sustainability Projects ALMA-35.00.101.666-A-SPE, NRAO, https://library.nrao.edu/public/memos/alma/main/memo602.pdf
Mangum, J. G., Baars, J. W. M., Greve, A., et al. 2006, PASP, 118, 1257
Mather, J. C., Fixsen, D. J., Shafer, R. A., Mosier, C., & Wilkinson, D. T. 1999, ApJ, 512, 511
Matsushita, S., Asada, K., Martin-Cocher, P. L., et al. 2017, PASP, 129, 025001
Matthews, L. D., Crew, G. B., Doeleman, S. S., et al. 2018, PASP, 130, 015002
Meledin, D., Lapkin, I., Fredrixon, M., et al. 2022, A&A, 668, A2
Mizuno, I., Friberg, P., Berthold, R., et al. 2020, Proc. SPIE, 11453, 114533T
Molod, A., Takacs, L., Suarez, M., & Bacmeister, J. 2015, GMD, 8, 1339
Moran, J. M., Ball, J. A., Hansen, S. S., et al. 1979, ApJL, 231, L67
Moran, J. M., Crowther, P. P., Burke, B. F., et al. 1967, Sci, 157, 676
Moritz, P., Nishihara, R., Wang, S., et al. 2017, arXiv:1712.05889
Natarajan, I., Deane, R., Martí-Vidal, I., et al. 2022, MNRAS, 512, 490

Padin, S., Woody, D. P., Hodges, M. W., et al. 1990, ApJL, 360, L11
Paine, S. 2022, The am Atmospheric Model, v12.2, Zenodo, doi:10.5281/zenodo.6774378
Pesce, D. W., Blackburn, L., Chaves, R., et al. 2024, ngEHT Simulation Tools, v1.0.0, Zenodo, doi:10.5281/zenodo.10722363
Planck Collaboration, Ade, P. A. R., Aghanim, N., et al. 2016, A&A, 594, A26
Potter, P. D. 1973, DSNPR, 16, 22
Raffin, P., Algaba-Marcosa, J. C., Asada, K., et al. 2014, Proc. SPIE, 9145, 91450G
Raymond, A. W., Palumbo, D., Paine, S. N., et al. 2021, ApJS, 253, 5
Readhead, A. C. S., Mason, C. R., Mofett, A. T., et al. 1983, Natur, 303, 504
Rienecker, M. M., Suarez, M. J., Gelaro, R., et al. 2011, JCli, 24, 3624
Rioja, M. J., & Dodson, R. 2020, A&ARv, 28, 6
Rioja, M. J., Dodson, R., & Asaki, Y. 2023, Galax, 11, 16
Roelofs, F., Blackburn, L., Lindahl, G., et al. 2023, Galax, 11, 12
Roelofs, F., Janssen, M., Natarajan, I., et al. 2020, A&A, 636, A5
Rusch, W. V. T., & Potter, P. D. 1970, Analysis of Reflector Antennas (New York: Academic Press)
Ruze, J. 1952, NCim, 9, 364
Ruze, J. 1966, IEEEP, 54, 633
Sekimoto, Y., Iizuko, Y., Satou, N., et al. 2008, Ninteenth Int. Symp. on Space Terahertz Technology, ed. W. Wild, 253, https://www.nrao.edu/meetings/isstt/papers/2008/2008253257.pdf
Stotskii, A. A. 1973, R&QE, 16, 620
Taylor, G. I. 1938, RSPSA, 164, 476
Thompson, A. R., Moran, J. M., & Swenson, G. W., Jr. 2017, Interferometry and Synthesis in Radio Astronomy (3rd ed.; Berlin: Springer)
Treuhaft, R. N., & Lanyi, G. E. 1987, RaSc, 22, 251
Vassilev, V., Meledin, D., Lapkin, I., et al. 2008, A&A, 490, 1157
Vertatschitsch, L., Primiani, R., Young, A., et al. 2015, PASP, 127, 1226
Virtanen, P., Gommers, R., Oliphant, T. E., et al. 2020, NatMe, 17, 261
Whitaker, J., Khrulev, C., Huard, D., et al. 2020, Unidata/netcdf4-python: version 1.5.5 release, v1.5.5rel2, Zenodo, doi:10.5281/zenodo.4308773
Whitney, A. R., Beaudoin, C. J., Cappallo, R. J., et al. 2013, PASP, 125, 196
Wielgus, M., Marchili, N., Martí-Vidal, I., et al. 2022, ApJL, 930, L19
Wilner, D. 1998, What is the Expected Sensitivity of the SMA? SMA Memo #125, Smithsonian Astrophysical Observatory, https://lweb.cfa.harvard.edu/sma/memos/125.pdf